Journal of Catalysis 319 (2014) 95–109

Contents lists available at ScienceDirect

Journal of Catalysis

journal homepage: www.elsevier.com/locate/jcat

Catalytic NO activation and NO–H_2 reaction pathways

David D. Hibbitts [a], Romel Jiménez [a,c], Masayuki Yoshimura [a,1], Brian Weiss [a,d], Enrique Iglesia [a,b,*]

[a] Department of Chemical Engineering, University of California, Berkeley, CA, United States
[b] E.O. Lawrence Berkeley National Laboratory, Berkeley, CA, United States
[c] Department of Chemical Engineering, University of Concepcion, Concepcion, Chile
[d] Corporate Research Strategic, Exxon Mobil Research and Eng. Co. Annandale, NJ, United States

ARTICLE INFO

Article history:
Received 7 May 2014
Revised 18 July 2014
Accepted 20 July 2014

Keywords:
Nitric oxide reduction
Platinum
Cluster size effects
Kinetic isotope effects
Density functional theory

ABSTRACT

Kinetic and isotopic data on Pt clusters and activation free energy barriers from density functional theory (DFT) on Pt(1 1 1) are used to assess the elementary steps involved in NO–H_2 reactions. Pt clusters 1–10 nm in diameter gave similar turnover rates, indicating that these elementary steps are insensitive to surface-atom coordination. N–O cleavage occurs after sequential addition of two chemisorbed H-atoms (H^*) to NO^* which are quasi-equilibrated with H_2 and NO co-reactants. The first step is equilibrated and forms HNO^*, while the second addition is irreversible and forms $^*HNOH^*$; this latter step limits NO–H_2 rates and forms OH^* and NH^* intermediates that undergo fast reactions to give H_2O, N_2O, NH_3, and N_2. These conclusions are consistent with (i) measured normal H/D kinetic isotope effects; (ii) rates proportional to H_2 pressure, but reaching constant values at higher pressures; (iii) fast H_2–D_2 equilibration during catalysis; and (iv) DFT-derived activation barriers. These data and calculations, taken together, rule out N–O cleavage via NO^* reactions with another NO^* (forming O^* and N_2O) or with vicinal vacancies (forming N^* and O^*), which have much higher barriers than H^*-assisted routes. The cleavage of N–O bonds via $^*HNOH^*$ intermediates is reminiscent of C–O cleavage in CO–H_2 reactions (via $^*HCOH^*$) and of O–O cleavage in O_2–H_2 reactions (via OOH^* or $^*HOOH^*$). H^*-addition weakens the multiple bonds in NO, CO, and O_2 and allows coordination of each atom to metal surfaces; as a result, dissociation occurs via such assisted routes at all surface coverages relevant in the practice of catalysis.

1. Introduction

Nitric oxide (NO) is a toxic by-product of combustion processes and must be removed from effluent streams via reduction processes on dispersed metal clusters. H_2, CO, NH_3, or hydrocarbons are often used as the reductants to form N_2 and H_2O as inert products and N_2O and NH_3 as undesired by-products [1–7]. H_2 becomes an attractive reductant when internal combustion engines can be tuned to form H_2 or when H_2 is produced via reforming or partial oxidation of a fuel side stream, because NO–H_2 reactions occur at temperatures typical of automotive exhaust streams (<500 K) [8–10]. Several studies have addressed catalytic NO–H_2 reactions [5,7–13] and the effects of CO_2, H_2O, and O_2 on rates and selectivities on Pt, Pd, and Rh catalysts [1,2,5,6]. These studies have led to contradictory conclusions about the identity and kinetic relevance of the required elementary steps and intermediates.

Previous kinetic studies of NO reduction by H_2 on supported noble metals concluded that molecular NO adsorption and dissociative H_2 adsorption are quasi-equilibrated [5,9–11]:

$$NO(g) + {}^* \rightleftharpoons NO^* \quad (1)$$

$$H_2(g) + 2^* \rightleftharpoons 2H^* \quad (2)$$

($\rightleftharpoons$ denotes a quasi-equilibrated reaction). The quasi-equilibrated nature of H_2 dissociation was inferred from dissociation rate constants on uncovered surfaces and NO–H_2 reaction rates [5,14] without direct evidence from H_2–D_2 equilibration during NO–H_2 reactions. Also, the identity of the most abundant surface intermediates (MASI) has remained equivocal. Infrared studies have shown that NO^* adsorbs molecularly at saturation coverages during NO–H_2 catalysis on Rh below 465 K (0.4–2.3 kPa NO) [5] and that the coverage of NO^* is unaffected by H_2 (1.1–12 kPa), indicating that NO^* is the sole MASI. Kinetic analysis of the effects of NO and H_2 pressures on turnover rates on Pt/$LaCoO_3$ and Pd/Al_2O_3 [9–11] was interpreted as evidence for the coexistence of vacancies (*), H^* and NO^*, a finding inconsistent with previous evidence on Rh [5]. N-containing species were estimated to cover 45–70% of the

* Corresponding author at: Department of Chemical Engineering, University of California, Berkeley, CA, United States.
E-mail address: iglesia@berkeley.edu (E. Iglesia).
[1] Current address: Corporate R&D Center (Toke), Showa Denko K.K., Japan

http://dx.doi.org/10.1016/j.jcat.2014.07.012
0021-9517/

Pt surface by isotopic measurements during NO–H_2 reactions at 400–460 K, with H^*, O^*, and OH^* as the other adsorbed species [8]. These previous studies provide qualitative agreement about the presence of NO^* at kinetically-consequential coverages, but without analogous consensus about H^* and * species.

The nature of the pathways that activate N–O bonds also remains controversial. Direct NO^* dissociation on vicinal vacant sites (*):

$$NO^* + * \rightarrow N^* + O^* \quad (3)$$

was reported as the kinetically-relevant step in H_2-free NO decomposition on Pt/Al_2O_3 at 523–573 K from pulse kinetic data [13,15], but NO decomposition reactions did not occur at 423 K [13]. Direct NO^* dissociation was also proposed to limit rates of NO–H_2–O_2 reactions on Pt–Mo–Co/α-Al_2O_3 at 415–433 K [16] and during NO–CO reactions on Rh/SiO_2 at 463–524 K [17]. Such conclusions are consistent with NO^* dissociation observed during adsorption measurements free of H_2 or CO co-reactants on Pt, Rh, and Pt-Rh single crystals [18–21]. Semiempirical calculations indicated that two adjacent chemisorbed NO^* molecules can react to form N_2O and O^* at low temperature (<573 K):

$$NO^* + NO^* \rightarrow N_2O + O^* + * \quad (4)$$

on Pt surfaces essentially saturated with NO^* [8,9,11], a mechanism previously proposed during single crystal studies on Pt and Rh [18]. This mechanism alone, however, cannot account for the formation of NH_3 or N_2 unless N_2O undergoes secondary reactions.

Neither direct NO^* dissociation (Eq. (3)) nor NO^*-assisted NO^* activation (Eq. (4)) as the sole kinetically-relevant steps can account for the observed increase in NO–H_2 turnover rates with increasing H_2 pressure on Rh/SiO_2 [5], $Pt/LaCoO_3$ [9] and Pd/Al_2O_3 [10,11]. Such H_2 effects have led to the proposal [5,9–11] that NOH^* species form and subsequently dissociate:

$$NO^* + H^* \rightarrow NOH^* + * \quad (5)$$

$$NOH^* + * \rightarrow N^* + OH^* \quad (6)$$

Either direct or H^*-assisted NO^* activation paths would lead to N^* as an intermediate in N_2 formation (via reaction with another N^*), N_2O (via reaction with NO^*), and NH_3 (via successive hydrogenation). Rate increases with increasing H_2 pressure has also been observed during CO–H_2 reactions on Fe, Co, [22] and Ru [23,24] catalysts, indicating that CO^* activation occurs only after the sequential addition of two H^*-species to form $^*HCOH^*$:

$$CO^* + H^* \rightleftharpoons HCO^* + * \quad (7)$$

$$HCO^* + H^* \rightarrow {}^*HCOH^* \quad (8)$$

followed by:

$$^*HCOH^* \rightarrow CH^* + OH^* \quad (9)$$

By analogy, we consider that H^*-assisted NO^* activation may occur via HNO^* and $^*HNOH^*$ intermediates with similar assistance by H^*:

$$NO^* + H^* \rightleftharpoons HNO^* + * \quad (10)$$

$$HNO^* + H^* \rightarrow {}^*HNOH^* \quad (11)$$

$$^*HNOH^* \rightarrow NH^* + OH^* \quad (12)$$

Once formed, NH^* can: (i) form NH_3 (via successive hydrogenation), (ii) dissociate to form N^* (and H^*) which can form N_2 (via reaction with another N^*) and N_2O (via reaction with NO^*), or (iii) react with NO^* to form $^*HNNO^*$ which goes on to form N_2O (following N–H activation) and N_2 (following sequential N–O and N–H activation) [25]. These diverse proposals for the mechanism of NO^* activation would lead to different activation energies and also to rate equations that would differ in their sensitivity to NO and H_2 pressures, thus allowing rate data and density functional theory calculations to discriminate among competing and often contradictory proposals for NO activation routes.

The effects of Pt particle size (and of concomitant changes in surface-atom coordination) on NO turnover rate and selectivity for NO–H_2 reactions have not been previously studied. Larger Pt and Rh particles bind NO^* [26–31] and H^* [15,29,32,33] more weakly than smaller particles because of the prevalence of low-index planes with exposed atoms of higher coordination on larger particles. Desorption rate data showed that NO^* dissociation occurs at lower temperatures on larger Pt particles (>4 nm compared to <2 nm), [30] indicating that NO–H_2 turnover rates may occur faster on larger clusters, possibly because vacancy formation is required during NO activation and more facile on larger clusters with lower NO^* binding energy. In the present study, we probe the effects of Pt surface-atom coordination on NO turnover rate by comparing NO–H_2 reaction rates on Pt clusters dispersed on γ-Al_2O_3 of varying size (1.5–10 nm diameter).

Here, we report kinetic, isotopic, and theoretical evidence for the identity and kinetic relevance of the elementary steps that mediate NO–H_2 reactions on Pt clusters (1.5–10 nm diameter) dispersed on γ-Al_2O_3. The effects of residence time on selectivity show that N_2, N_2O, and NH_3 form during one surface sojourn and do not react further or inhibit NO–H_2 reactions. H_2–D_2 isotopic exchange rates during reaction showed that H_2 dissociation is equilibrated; the observed kinetic effects of NO and H_2 indicate that NO reduction occurs via H^*-assisted routes on surfaces predominantly covered by NO^* and H^* (MASI). These conclusions were confirmed by estimates of activation barriers using density functional theory (DFT). NO^* reacts with H^* to form HNO^* in a quasi-equilibrated step and adds another H^* to form $^*HNOH^*$ in the kinetically-relevant step. NO activation turnover rates increased slightly with increasing Pt cluster diameter (1.5–10 nm) (1.5–1.7 factors at 383–453 K), indicating that Pt–N and Pt–H bond strengths vary to similar extents with changes in surface metal atom coordination.

2. Experimental methods

2.1. Catalyst synthesis and characterization protocols

γ-Alumina (Sasol Catalox, SBa-200, 150 $m^2\ g^{-1}$) was treated in flowing dry air (Praxair, extra dry, 1 $cm^3\ s^{-1}\ g^{-1}$) at 1023 K for 4 h before incipient wetness impregnation with $Pt(NH_3)_4(NO_3)_2$ (Alfa Aesar, 99.99%) solutions in deionized water. The Pt concentration in the solution was adjusted to give catalysts with 0.6, 1.1, and 1.2 wt.% Pt content. Precursor solutions were added dropwise to Al_2O_3 (3–5 g; 0.5 $cm^3\ g^{-1}$). Impregnated samples were treated in stagnant ambient air at 393 K for 4 h and then in flowing dry air (Praxair, extra dry, 1 $cm^3\ s^{-1}\ g^{-1}$) at 823 K for 4 h. Samples were treated in flowing dry air (1 $cm^3\ s^{-1}\ g^{-1}$) at different temperatures for 4 h to obtain catalysts with different Pt dispersions as shown in Table 1.

Fractional Pt dispersions were measured from irreversible H_2 chemisorption uptakes at 313 K (Quantachrome Autosorb-1) at 3–50 kPa H_2. H_2 adsorption isotherms were measured on samples treated in pure H_2 (Praxair, 99.999%, 50 $cm^3\ g^{-1}\ s^{-1}$; 1 bar) by heating from ambient temperature to 673 K at 0.083 K s^{-1} and holding for 1 h, followed by evacuation to 10^{-3} Pa at 673 K for 1 h. A second isotherm was measured after evacuation at 313 K for 0.5 h to measure the uptakes of weakly-bound hydrogen. Pt dispersions were determined from the difference between these two isotherms, each extrapolated to zero H_2 pressure, using 1:1 H:Pt adsorption stoichiometry [25]. Mean Pt cluster sizes were estimated from these dispersion values by assuming hemispherical

Table 1
Pt content, treatment temperature and dispersions of Pt/Al_2O_3.

Catalyst	Pt content (wt.%)	Treatment temperature (K)[a]	Dispersion[b]	Mean particle diameter (nm)[c]
A	1.1	773	0.63	1.7
B	0.6	823	0.25	4.4
C	1.2	973	0.08	13.7

[a] In flowing dry air (1 $cm^3\ s^{-1}\ g^{-1}$) for 4 h.
[b] From H_2 chemisorption at 313 K.
[c] From fractional dispersion based on hemispherical particles and a bulk Pt density (21.45 g cm^{-3}).

clusters with the density of bulk Pt metal (21.45 g cm^{-3}). The 0.6 wt.% Pt/Al_2O_3 catalyst gave a dispersion of 0.25, corresponding to a mean particle diameter of 4.4 nm as shown in Table 1. This catalyst was used for the results shown in Sections 3.1-3.4.

2.2. Steady-state reaction rate measurements

Reactant gases (99.999% purity) were obtained from Praxair (1.0% NO/0.52% Ar/He, 10% H_2/He, 0.999% N_2O/He, 0.999% NH_3/He). He (Praxair, 99.999%) was used as an inert carrier. The concentrations of NO, N_2O, and NH_3 in the inlet and outlet streams were measured using an infrared analyzer (MultiGas 2030, MKS Instruments). The outlet concentration of N_2 was estimated by the nitrogen balance using infrared analysis data and by mass spectrometry (Mini-Lab, MKS). H_2O and H_2 concentrations were determined from oxygen and hydrogen balances, respectively.

Rate and selectivity data were obtained on catalysts mixed with γ-alumina and then sieved to retain particles 150–180 μm in diameter. Such intrapellet dilution ensured the absence of intrapellet concentration or temperature gradients, while preventing detectable pressure drops. Samples were held onto a porous quartz disk (6 mm) within a quartz tube (6 mm). They were heated to 523 K at 0.2 K s^{-1} in flowing He (Praxair, 99.999%, 10 $cm^3\ s^{-1}\ g^{-1}$), exposed to 10% H_2/He (Praxair, 99.999%, 10 $cm^3\ s^{-1}\ g^{-1}$) at 523 K for 1 h, and then to the reactants (0.3 kPa NO/1.5 kPa H_2/He; 10 $cm^3\ s^{-1}\ g^{-1}$) at 383 K for >1 h before rate measurements. Rates were measured at temperatures between 383 K and 453 K for inlet streams containing NO (0.05–0.6 kPa) and H_2 (0.15–760 kPa) with He as balance. Rates were measured at a set condition (0.3 kPa NO, 1.5 kPa H_2) in between each change in reactant concentrations to ensure that deactivation or catalyst changes did not influence kinetic effects. NO conversions were kept below 15%, and all rates were analyzed based on a differential reactor. N_2 formation rates were determined by difference from measured rates of NO consumption and of N_2O and NH_3 formation (by infrared analyzer), and confirmed by mass spectrometry. NO consumption and N_2O, NH_3, and N_2 formation rates are reported as molecular rates of consumption or formation divided by the surface Pt atoms [mol (mol Pt_{surf})$^{-1}$ s^{-1}].

NO consumption rates were measured on samples with different intrapellet and bed dilution ratios (from 1:50 to 1:200 catalyst:alumina), and no effects of dilution were detected, consistent with rate data of strict kinetic origins and without heat or mass transport artifacts. A 1:200 catalyst:alumina dilution ratio was used for all rate measurements in this study.

2.3. H_2–D_2 isotopic exchange rates and kinetic isotope effects

H_2/D_2 isotopic exchange rates (0.75 kPa H_2, 0.75 kPa D_2) were measured on Pt/Al_2O_3 at 383–503 K and 0–0.5 kPa NO at total flow rates of 5–50 $cm^3\ s^{-1}\ g^{-1}$. D_2/H_2 kinetic isotope effects (KIE) were measured on Pt/Al_2O_3 at 423 K for inlet streams containing H_2 (1–3 kPa), D_2 (2–12 kPa) and NO (0.1–0.5 kPa), with Ar as internal standard (0.15 kPa) and He as balance at total flow rates between 5 and 25 $cm^3\ s^{-1}\ g^{-1}$.

2.4. Density functional theory methods

First-principles density functional theory (DFT) calculations were performed using the Vienna ab initio simulation package (VASP) [34–37]. Planewaves were constructed with an energy cutoff of 396 eV using projector-augmented wave (PAW) methods [38,39] with correlation and exchange energies from the revised Perdew–Burke–Ernzerhof (RPBE) functional [40–42]. Vacuum-phase calculations were carried out within a 1.8 × 1.8 × 1.8 nm unit cell with the Pt(1 1 1) surface modeled as 2-dimensional slabs composed of a 3 × 3 surface mesh and four atomic metal layers with a 1 nm vacuum region between the slabs. The bottom two layers were frozen in their bulk crystallographic positions and the top two layers were fully relaxed. Wavefunctions were converged to within 10^{-6} eV with a 3 × 3 × 1 Monkhorst–pack sampling of the first Brillouin zone (k-point mesh) [43]. Optimizations were carried out without spin polarization until the force on any atom was weaker than 0.05 eV/Å; forces were computed using a fast Fourier transform (FFT) grid with a cutoff of twice the planewave cutoff. After structural convergence, a single-point energy calculation was performed with a 6 × 6 × 1 k-point mesh for all reactant, product, and transition states.

Transition states were identified using a two-step process. The minimum energy pathway (MEP) was first determined using the NEB method [44,45], and converged to within 0.3 eV/Å; this pathway was then used to initiate a Dimer calculation [46], which was converged to within 0.05 eV/Å. After convergence, a single-point energy calculation was performed for all species at a 6 × 6 × 1 k-point mesh.

Frequency calculations were performed on all optimized states to determine zero-point vibrational energies (*ZPVE*), vibrational enthalpies (H_{vib}), and free energies (G_{vib}). These terms were then used, along with electronic energies (E_0, provided by VASP), to estimate enthalpies:

$$H = E_0 + ZPVE + H_{vib} + H_{trans} + H_{rot} \quad (13)$$

and free energies:

$$G = E_0 + ZPVE + G_{vib} + G_{trans} + G_{rot} \quad (14)$$

for all reactant, product, and transition states. For gaseous molecules, translational and rotational enthalpies and free energies were also computed from statistical mechanics. Equations for *ZPVE*, H_{vib}, and G_{vib} from vibrational frequencies and H_{trans}, H_{rot}, G_{trans}, and G_{rot} for gas-phase molecules are reported in the Supporting Information (SI), Eqs. (S1)–(S11).

Intrinsic enthalpy and free energy barriers (ΔH_{act} or ΔG_{act}, respectively) denote differences in enthalpy or free energy between a transition state and its precursor reactants for an elementary step. For instance, in the case of $^*HNOH^*$ formation from HNO^* and H^* (Eq. (11)):

$$\Delta G_{act,11} = G[HNO{-}H^{\ddagger **}] - G[HNO^*] - G[H^*] \quad (15)$$

Reaction enthalpies and free energies denote differences between the products and reactants for an elementary step. For instance, in the case of $^*HNOH^*$ formation from HNO^* and H^* (Eq. (11)):

$$\Delta G_{rxn,11} = G[HNOH^{**}] - G[HNO^*] - G[H^*] \quad (16)$$

Effective activation enthalpies ($\Delta H^{\ddagger}$) and free energies ($\Delta G^{\ddagger}$) denote here the sum of intrinsic enthalpy and free energy barriers (ΔH_{act} or ΔG_{act}, respectively) and the reaction energies for all steps necessary to form the precursor reactants from a NO^*-covered surface. For instance, in the case of $^*HNOH^*$ formation (Eq. (11)): NO^* desorbs,

2 H* adsorb, and HNO* is formed (from NO* and H*, Eq. (10)) to form the HNO* and H* reactants. The $\Delta G^{\ddagger}$ for this reaction includes the desorption free energy of NO* ($\Delta G_{ads,NO}$, Eq. (1)), adsorption free energy of H_2 ($\Delta G_{ads,H2}$, Eq. (2)), reaction free energy of HNO* formation ($\Delta G_{rxn,10}$, Eq. (10)), and intrinsic free energy barrier for Eq. (11) ($\Delta G_{act,11}$):

$$\Delta G^{\ddagger} = \Delta G_{act,11} - \Delta G_{ads,NO} + \Delta G_{ads,H2} + \Delta G_{rxn,10} \quad (17)$$

By substituting in free energies of individual species, one can see that the free energies of reactive intermediates (such as H* and HNO*) have no effect on $\Delta G^{\ddagger}$:

$$\Delta G^{\ddagger} = G[\mathrm{HNO{-}H^{\ddagger **}}] + G[\mathrm{NO(g)}] - 2G[\mathrm{NO^*}] - 2G[\mathrm{H_2(g)}] \quad (18)$$

Calculated $\Delta H^{\ddagger}$ and $\Delta G^{\ddagger}$ values can then be compared to those derived from measured NO–H_2 reaction rates and their temperature-dependences.

3. Results and discussion

3.1. Effects of product concentration on NO–H_2 reaction rates

N_2O, N_2, and NH_3 formation rates did not depend on residence time or the extent of NO conversion (Figs. 1 and S1 in SI) at 383, 423, and 453 K, indicating that all products form via primary pathways during one surface sojourn and that they do not inhibit NO conversion reactions or undergo secondary interconversions.

N_2O neither reacts during NO–H_2 reactions nor inhibits such reactions at 383 K or 453 K (Figs. 2a and S2); N_2O reactions with H_2 (in the absence of NO) were much slower than reactions of NO with H_2 at the same reactant pressures. NH_3 reacts with NO in the absence of H_2, but NH_3 did not influence NO–H_2 reaction rates (Fig. 2b). The addition of H_2O at pressures higher than those prevalent during NO–H_2 reactions (0.5–3.0 kPa) did not detectably affect reaction rates (Fig. 3). These data, taken together with the absence of residence time effects on rates or selectivities, show that all products form via primary pathways and that neither inhibition by products nor their secondary interconversions influence any of the rates and selectivities reported here.

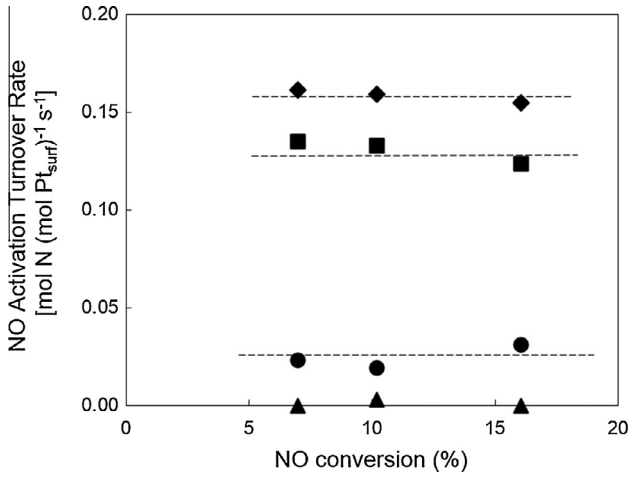

Fig. 1. Effect of space velocity on NO consumption rates at 383 K during NO/H_2 reactions on 0.6%Pt/Al_2O_3 (4 nm average particle diameter); NO consumption (♦), N_2O formation (■), N_2 formation (●), NH_3 formation (▲). (0.3 kPa NO; 1.5 kPa H_2) Fig. S1 (SI) contains data at 423 K and 453 K.

3.2. Effects of NO and H_2 concentrations on NO activation rates

NH_3, N_2, and N_2O products are formed following kinetically-relevant NO* activation through a common intermediate, the details of which are discussed in this study. This common intermediate then goes on to form NH_3, N_2, and N_2O in kinetically-invisible branching steps which determine the selectivity of NO–H_2 reactions on Pt [25]. Thus, NO activation rates (r_{NO}) are given by the sum of product molar formation rates:

$$r_{NO} = r_{NH_3} + r_{N_2O} + r_{N_2} \quad (19)$$

NO activation turnover rates decreased monotonically with increasing NO pressure and were proportional to H_2 pressure at low H_2 pressures (<5 kPa) (383 K; Fig. 4a). At higher H_2 pressures (>5 kPa), however, NO–H_2 reaction rates increased with increasing H_2 and NO pressures (Fig. 4b), and similar trends were observed at 453 K (Fig. 5a). NO conversion rates ultimately became independent of H_2 pressure at higher pressures (398 K; Fig. 5b).

3.3. Isotopic H_2–D_2 exchange as evidence for quasi-equilibrated H_2 dissociation

Plausible mechanistic interpretations for these positive effects of H_2 include the following: (i) H_2 dissociation as the sole kinetically-relevant step or (ii) quasi-equilibrated H_2 dissociation followed by kinetically-relevant steps involving reactions of H-atoms with NO-derived intermediates. H_2 dissociation (Eq. (2)) was previously assumed to be quasi-equilibrated during NO–H_2 reactions on Pt [13] based on the rapid nature of H_2/D_2 exchange in the absence of NO [5,6,9,13]. Such conclusions, however, are flawed because the reversibility of H_2 dissociation during NO–H_2 reactions cannot be determined in the absence of NO* as doing so ignores any effects of NO* on the intrinsic rates of H* recombinative desorption and cannot be used to compare such rates to H* reactions with NO-derived intermediates.

The reversibility of H_2 dissociation steps was probed by comparing H*/D* recombination rates during H_2/D_2 exchange in the presence of NO:

$$r_{H^*\text{-equil}} = 2r_{HD} \quad (20)$$

with H*/D* consumption rates in NO reduction reactions as:

$$r_{H^*\text{-react}} = r_{N_2O} + 2r_{N_2} + \frac{5}{2} r_{NH_xD_{3-x}} \quad (21)$$

Quasi-equilibrated H_2 dissociation (Eq. (2)) would lead to large $r_{H^*\text{-equil}}/r_{H^*\text{-react}}$ ratios, while irreversible dissociation would give values much smaller than unity. At all conditions examined, $r_{H^*\text{-equil}}/r_{H^*\text{-react}}$ ratios were larger than unity, consistent with quasi-equilibrated H_2 dissociation steps (Fig. 6). The ratio of H_2–D_2 to NO reduction rates increased with temperature and with increasing H_2/NO ratios, because such changes increase H*/NO* ratios at surfaces and thus the rate of recombinative H_2 desorption over that of H* reactions with NO*. Such direct evidence shows that the observed effects of H_2 pressure on NO reaction rates must reflect the involvement of H* atoms in the formation of the kinetically-relevant transition state, presumably via the addition of one or more H* to NO-derived intermediates.

3.4. Plausible functional forms of NO–H_2 rate equations and mechanistic inferences

The positive effects of NO pressure on rates at high H_2 pressures (Fig. 5a) and their initial proportional increase with H_2 pressure at low H_2 pressures (Fig. 4a) are consistent with a kinetically-relevant transition state containing one NO* (or NO*-derived intermediate) and two H-atoms. Direct NO* activation (Eq. (3)) is unlikely to be

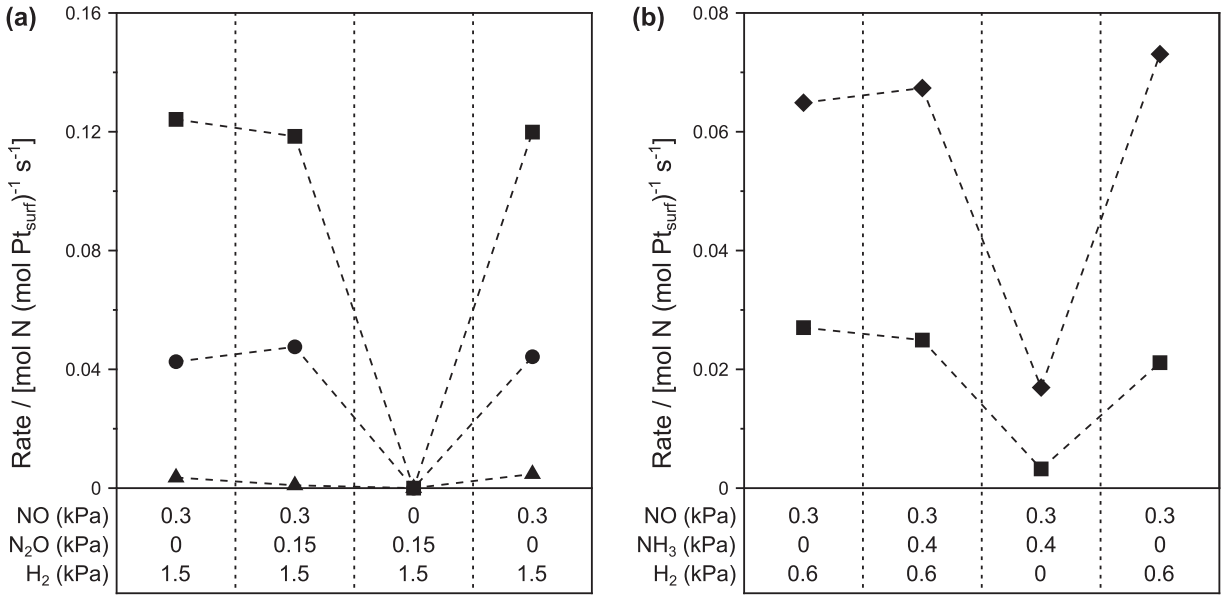

Fig. 2. Effects of (a) N_2O and (b) NH_3 product addition on rates of formation of N_2O (■), N_2 (●), and NH_3 (▲); as well as rate of consumption of NO (♦) (mol N (mol Pt_{surf})$^{-1}$ s^{-1}). (383 K, 0.6 wt.% Pt/Al_2O_3 (4 nm average particle diameter), 8.3 cm^3 s^{-1} g^{-1}, 0.3 kPa NO, 0.4 kPa NH_3, 0.6 kPa H_2). Fig. S2 (SI) shows data at 453 K.

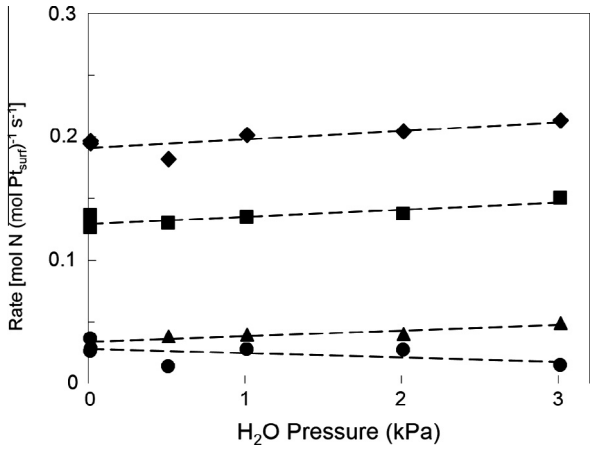

Fig. 3. Effects of H_2O addition on rates of: NO consumption (♦), N_2O formation (■), N_2 formation (●), and NH_3 formation (▲) (mol N (mol Pt_{surf})$^{-1}$ s^{-1}) (383 K, 0.6 wt.% Pt/Al_2O_3 (4 nm average particle diameter), 5.6 cm^3 s^{-1} g^{-1}, 0.1 kPa NO, 1.5 kPa H_2, 0–3 kPa H_2O).

quasi-equilibrated at these conditions (as discussed below and in [8–11,17]). If irreversible direct NO* dissociation was the prevalent mechanism for NO* activation, the kinetically-relevant transition state would not contain any H-atoms, making such routes inconsistent with the observed H_2 kinetic effects. The apparent first-order rate dependence on H_2 pressure suggests a H*-assisted NO* activation route via HNO* in which its formation (Eq. (10)) is quasi-equilibrated and a subsequent H* addition step to form *HNOH* (Eq. (11)) is irreversible. These H-assisted routes are analogous, in their use of co-adsorbed species instead of vacant sites, to those recently proposed to account for the activation of CO* via *HCOH* intermediates in CO–H_2 reactions on Fe, Ru, or Co catalysts [23,24]; such bimolecular assistance appears to prevail over direct monomolecular routes on crowded surfaces, which are ubiquitous during catalytic reactions at conditions relevant to their practice.

The observed inhibition effects by NO at low H_2 pressures (Fig. 4a) and the gradual saturation of H_2 kinetic effects at high H_2 pressures (Fig. 5b) indicate that NO* and H* coexist at kinetically-relevant concentrations, leading to the appearance of terms that depend on H_2 and NO pressures in the denominator of the rate equation:

$$r_{NO} = \frac{k_{11}K_{10}K_{NO}K_{H_2}P_{NO}P_{H_2}}{\left[1 + K_{NO}P_{NO} + \left(K_{H_2}P_{H_2}\right)^{0.5}\right]^2} \quad (22)$$

Here, k_{11} is the rate constant for H*-addition to HNO* to form *HNOH* (Eq. (11)) and K_{10}, K_{NO}, and K_{H_2} are the equilibrium constants for HNO* formation (Eq. (10)), molecular NO chemisorption (Eq. (1)), and dissociative H_2 chemisorption (Eq. (2)). K_{NO}, K_{H_2}, and $k_{11}{\cdot}K_{10}$ values at 383, 423, and 453 K (Table 2) were regressed using rate data by minimizing the sum of relative errors (SRE, Eq. S13) through non-linear parameter estimation protocols.

A parameter sensitivity analysis (SI) was performed by re-regressing Eq. (22) over a large range of fixed K_{H_2} values and indicated that the values of K_{H_2}, K_{NO} and $k_{11}{\cdot}K_{10}$ cannot be independently determined, but their ratios can be accurately measured (e.g., the ratio of $K_{H_2}^{0.5}$ to K_{NO} is 0.110, at 383 K shown in SI, Fig. S4) because the terms $K_{NO}P_{NO}$ and $(K_{H_2}P_{H_2})^{0.5}$ in the denominator of Eq. (22) are much larger than 1, indicating that vacant sites are kinetically-undetectable during steady-state catalysis at the conditions of these experiments. As a result, Eq. (22) becomes:

$$r_{NO} = \frac{\alpha P_{NO}P_{H_2}}{\left[P_{NO} + \beta P_{H_2}^{0.5}\right]^2} \quad (23)$$

Eq. (23) contains only two parameters:

$$\alpha = \frac{k_{11}K_{10}K_{H_2}}{K_{NO}} \quad (24)$$

$$\beta = \frac{K_{H_2}^{0.5}}{K_{NO}} \quad (25)$$

and values of α and β at 383, 423, and 453 K (Table 3) were regressed using rate data by minimizing the SRE through non-linear parameter estimation protocols.

These regressed parameters accurately describe all measured NO–H_2 turnover rates (Fig. 7).

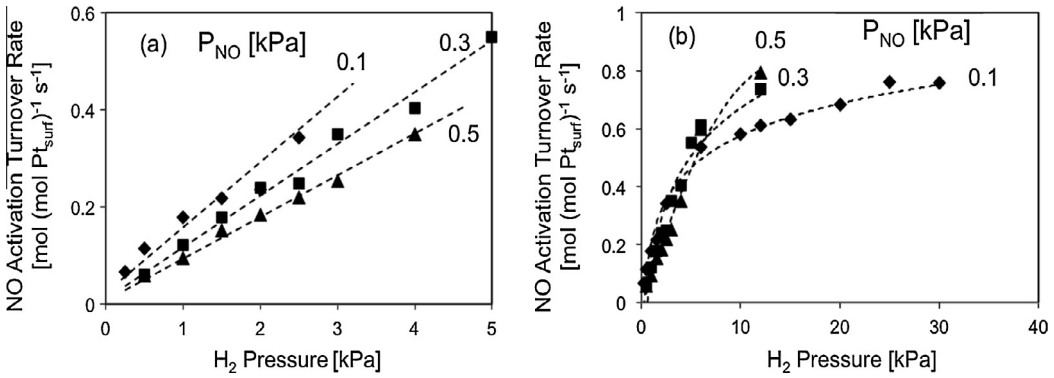

Fig. 4. Effect of H_2 pressure on NO consumption turnover rates at NO pressures of 0.1 kPa (♦), 0.3 kPa (■), and 0.5 kPa (▲) (0.6%Pt/Al_2O_3, 4 nm average particle diameter, 383 K); (a) low H_2 pressures (0.25–5 kPa), (b) high H_2 pressures (0.25–30 kPa).

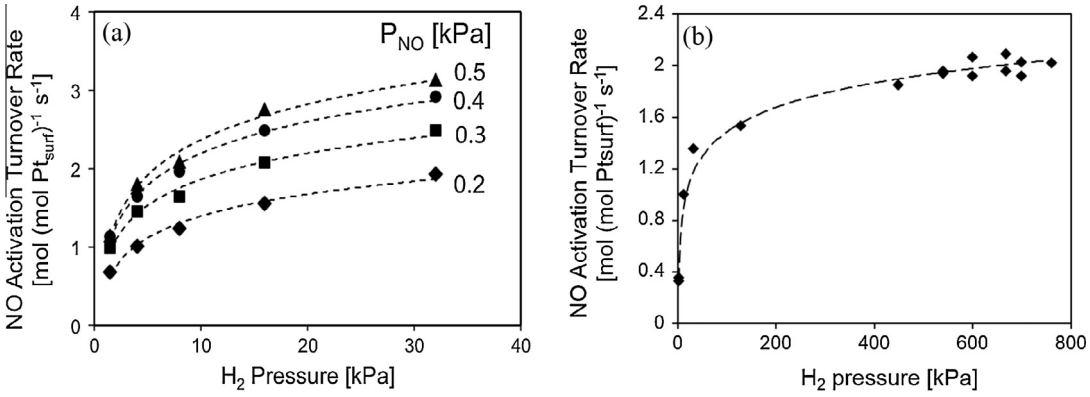

Fig. 5. Effect of H_2 pressure on NO consumption turnover rates (a) at 453 K and NO pressures of 0.1 kPa (♦), 0.3 kPa (■), 0.4 (●), and 0.5 kPa (▲), and (b) at 398 K and high H_2 pressures and 0.2 kPa NO (0.6 wt.% Pt/Al_2O_3, 4 nm average particle diameter, 1.5–760 kPa H_2).

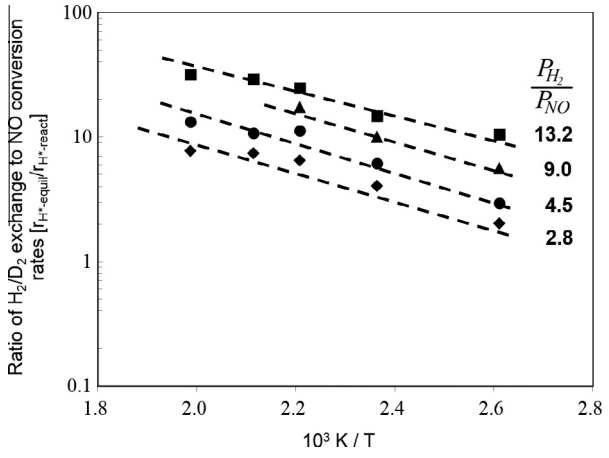

Fig. 6. Arrhenius plots of H/D exchange to NO conversion rate ratio ($r_{H^*\text{-equil}}/r_{H^*\text{-react}}$) for NO reduction with H_2/D_2 isotopic exchange at different hydrogen coverages (0.6%Pt/Al_2O_3, 4 nm average particle diameter, 383 K, 0.1–0.3 kPa NO, 0.5–1.0 kPa H_2 or D_2).

Alternate sequences of elementary steps, such as those involving irreversible direct NO* activation (Eq. (3)) or kinetically-relevant transition states containing only one H-atom (Eq. (5) or Eq. (6)), lead to rate equations inconsistent with measured rates (Table S1 shows regressed parameters and errors for such alternate routes). For instance, kinetically-relevant NOH* dissociation steps (Eq. (6)) would give the rate equation:

Table 2
Regressed kinetic parameters for Eq. (22).

Temperature (K)	$k_{11}\cdot K_{10}$ (s^{-1} kPa^{-2})	K_{NO} (kPa^{-1})	K_{H_2} (kPa^{-1})	SRE
383	683	76.5	69.6	151
423	465	30.5	44.2	92
453	366	17.0	33.2	136

$$r_{NO} = \frac{\alpha' P_{NO} P_{H_2}^{0.5}}{\left[1 + K_{NO} P_{NO} + K_{H_2}^{0.5} P_{H_2}^{0.5}\right]^2} \quad (26)$$

This equation describes measured rates much less accurately (862, SRE) than Eq. (22) or Eq. (23) (380, 401, SRE). In fact, turnover rates reach constant asymptotic values at H_2 pressures above 400 kPa (Fig. 5b), consistent with the functional form of Eq. (23). In contrast, the form of Eq. (26) at high H_2 pressures:

$$r_{NO} = \frac{\alpha P_{NO}}{K_{H_2} P_{H_2}^{0.5}} \quad (27)$$

depends inversely on H_2 pressure, in contradiction to the rate data in Fig. 5b.

The elementary steps (Eqs. (1), (2), (10) and (11)) and assumptions used to derive Eq. (23) provide the mechanistic basis required to determine the chemical origins of the α and β lumped parameters. The thermodynamic constant, β (Eq. (25)), contains the equilibrium constant for NO* (K_{NO}^{-1}, Eq. (1)) and H* adsorption

Table 3
Regressed kinetic parameters for Eq. (23).

Temperature (K)	α (s^{-1})	β ($kPa^{-0.5}$)	SRE
383	0.112	0.110	159
423	0.426	0.206	91
453	1.002	0.307	151

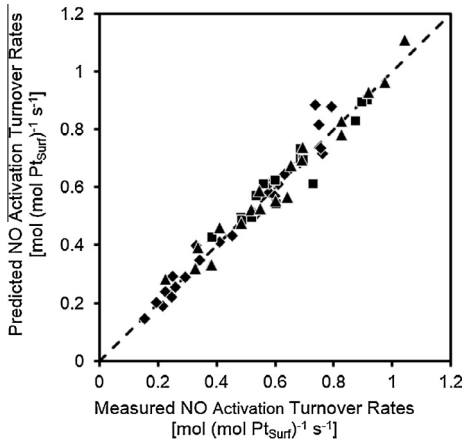

Fig. 7. Measured and predicted NO activation turnover rates (Eq. (23)) with kinetic parameters shown in Table 3 for NO–H_2 reactions at 383 K (♦), 423 K (■), and 453 K (▲) on 0.6 wt.% Pt/Al_2O_3 (4 nm average particle diameter).

($K_{H_2}^{0.5}$). These values of β depend on the difference in free energy ($\Delta\Delta G_{ads}$) between these two adsorption steps:

$$\beta(\text{bar}^{0.5}) = \frac{K_{H_2}^{0.5}}{K_{NO}} = e^{\left(\frac{-\Delta\Delta G_{ads}}{RT}\right)} \quad (28)$$

and reflect the difference between the H_2 adsorption free energy per mole of H* ($0.5\Delta G_{ads,H_2}$) and the NO* adsorption free energy ($\Delta G_{ads,NO}$):

$$\Delta\Delta G_{ads} = \left(0.5G_{ads,H_2} - G_{ads,NO}\right) \quad (29)$$

which reflects, in turn, the free energy change associated with replacing one NO* with one H* (Fig. 8); it has a value of 14 kJ mol^{-1} at 1 bar H_2 and NO and 423 K on 0.6 wt.% Pt/Al_2O_3 (4 nm average particle diameter). The temperature-dependence of β (Fig. 9):

$$\Delta\Delta G_{ads} = \Delta\Delta H_{ads} - T\Delta\Delta S_{ads} \quad (30)$$

gives a $\Delta\Delta H_{ads}$ value of 21 kJ mol^{-1} and a $\Delta\Delta S_{ads}$ value of 18 J mol^{-1} K^{-1}:

$$\Delta\Delta H_{ads} = \left(0.5\Delta H_{ads,H_2} - \Delta H_{ads,NO}\right) \quad (31)$$

$$\Delta\Delta S_{ads} = \left(0.5\Delta S_{ads,H_2} - \Delta S_{ads,NO}\right) \quad (32)$$

Thus, the replacement of NO* with H* (Fig. 8a) gives rise to a loss in free energy, as a result of a loss in enthalpy and a concomitant gain in entropy (at 1 bar). $\Delta\Delta H_{ads}$ can be rewritten in terms of the binding energies of H* and NO*:

$$\Delta\Delta H_{ads} = BE(H^*) + 0.5BDE(H_2) - BE(NO^*) \quad (33)$$

where BE is the binding energy and BDE(H_2) is the bond dissociation energy of H_2(g) (436 kJ mol^{-1}). Eq. (33) indicates that the H* binding energy is 197 kJ mol^{-1} stronger than the NO* binding energy. $\Delta\Delta S_{ads}$ can be rewritten in terms of entropies of H*, NO*, H_2 and NO:

$$\Delta\Delta S_{ads} = S[H^*] - 0.5S[H_2] + S[NO] - S[NO^*] \quad (34)$$

The known entropies of gaseous H_2 and NO molecules (141 J mol^{-1} K^{-1} and 210 J mol^{-1} K^{-1} at 423 K and 1 bar, respectively) taken together with measured $\Delta\Delta S_{ads}$ values indicate that H* has less entropy (by 122 J mol^{-1} K^{-1}) than NO* because NO* has more mass than H* and vibrational entropy is proportional to reduced mass. DFT-derived H_2 dissociation enthalpies ($\Delta H_{ads,H_2}$) on Pt(111) decreased from −64 kJ mol^{-1} to −26 kJ mol^{-1} as H* coverages increased from 1/9 to 1 monolayer (ML, defined as H*/Pt_{surf} = 1) (SI, Fig. S6). $\Delta H_{ads,H_2}$ were similar for all symmetrically unique configurations of H* at each coverage (Fig. S7–S9), indicating that H*–H* repulsion is because of through-metal interactions, rather than direct through-space interactions. Similarly, NO adsorption weakened as NO* coverages increased from 1/9 to 1 ML ($\Delta H_{ads,NO}$ varied from −136 kJ mol^{-1} to +45 kJ mol^{-1}) (SI, Fig. S10). $\Delta H_{ads,NO}$ varied strongly among distinct configurations of NO* on the surface at intermediate coverages, even if binding modes of NO* were not altered (Figs. S11–S13). This indicates that NO*–NO* repulsions are a combination of through-metal and through-space interactions. NO* coverage effects are stronger than H* coverage effects, because of the larger size and thus stronger through-space repulsion among NO* species. These through-space repulsions are likely to be overestimated by these DFT methods, as they do not include dispersive interactions, such as van der Waals forces likely to partially offset Pauli repulsions. $\Delta\Delta H_{ads}$ and $\Delta\Delta G_{ads}$ values were calculated on saturated surfaces at 1/9–1 ML NO* coverage with H* occupying all other sites (Fig. S14). Calculated $\Delta\Delta H_{ads}$ values are closest to measured values (21 kJ mol^{-1}) at 5/9 ML NO* and 4/9 ML H* (36 kJ mol^{-1}), and calculated $\Delta\Delta G_{ads}$ values are closest to measured values (14 kJ mol^{-1}) at 4/9 ML NO* and 5/9 ML H* (16 kJ mol^{-1}). Calculated $\Delta\Delta H_{ads}$ and $\Delta\Delta G_{ads}$ values change dramatically with coverage, ranging from 69 to −47 kJ mol^{-1} and 34 to −95 kJ mol^{-1}, respectively, from 1/9–1 ML NO* (with H* occupying all other sites) indicating that it is easier to replace NO* with H* on the surface as NO* coverage increases. These large coverage effects are inconsistent with the Langmuir–Hinshelwood assumptions embedded within Eq. (23) (and thus the definition of β), weakening direct comparisons between calculated and measured $\Delta\Delta H_{ads}$ and $\Delta\Delta G_{ads}$ values.

The lumped parameter α (Eq. (24)) contains thermodynamic constants for quasi-equilibrated NO adsorption (K_{NO}^{-1}, Eq. (1)), H_2 dissociation (K_{H_2}, Eq. (2)), and HNO* formation (K_{10}, Eq. (10)) and kinetic constants for irreversible *HNOH* formation (k_{11}, Eq. (11)). The values of α (Fig. 9) depend on an effective free energy barrier ($\Delta G^{\ddagger}$) given by:

$$\alpha = \frac{k_{11}K_{10}K_{H_2}}{K_{NO}} = \frac{k_B T}{h} e^{\left(\frac{-\Delta G^{\ddagger}}{RT}\right)} \quad (35)$$

where $\Delta G^{\ddagger}$ depends on free energies for NO* ($\Delta G_{ads,NO}$) and H_2 adsorption ($\Delta G_{ads,H_2}$), on the reaction free energy for HNO* formation ($\Delta G_{rxn,10}$), and on the free energy barrier ($\Delta G_{act,11}$) for the formation of the kinetically-relevant transition state from HNO* and H*:

$$\Delta G^{\ddagger} = -\Delta G_{ads,NO} + \Delta G_{ads,H_2} + \Delta G_{rxn,10} + \Delta G_{act,11} \quad (36)$$

The measured value of α (Fig. 9) at 423 K corresponds to a $\Delta G^{\ddagger}$ value of +108 kJ mol^{-1} and its temperature-dependence:

$$\Delta G^{\ddagger} = \Delta H^{\ddagger} - T\Delta S^{\ddagger} \quad (37)$$

gives a $\Delta H^{\ddagger}$ value of +42 kJ mol^{-1}, where $\Delta H^{\ddagger}$ is defined as:

$$\Delta H^{\ddagger} = -\Delta H_{ads,NO} + \Delta H_{ads,H_2} + \Delta H_{rxn,10} + \Delta H_{act,11} \quad (38)$$

The corresponding $\Delta S^{\ddagger}$ value is −156 J mol^{-1} K^{-1} (Eq. (37)), where $\Delta S^{\ddagger}$ is defined as:

$$\Delta S^{\ddagger} = -\Delta S_{ads,NO} + \Delta S_{ads,H_2} + \Delta S_{rxn,10} + \Delta S_{act,11} \quad (39)$$

Eq. (36) (and analogous equations for $\Delta H^{\ddagger}$ and $\Delta S^{\ddagger}$) can be rewritten in terms of the energies of the species involved:

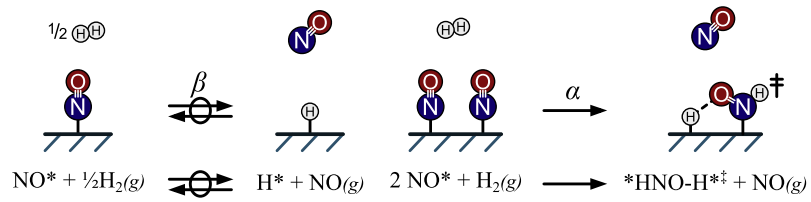

Fig. 8. Reactions corresponding to (a) the thermodynamic parameter β and (b) the kinetic parameter α.

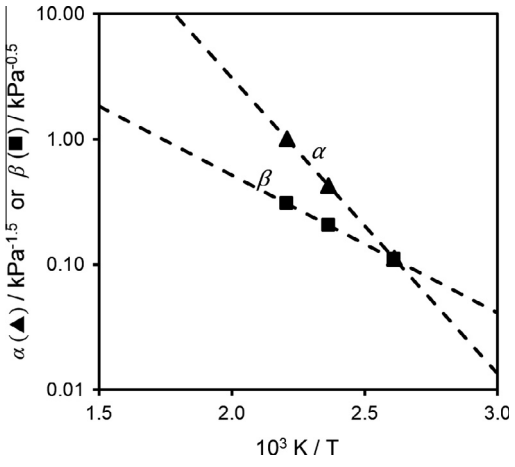

Fig. 9. Temperature-dependence of α (▲) and β (■) at 383–503 K on 0.6% Pt/Al_2O_3 (4.4 nm average particle diameter).

$$\Delta G^{\ddagger} = G[TS^{2*}] + G[NO_{gas}] - 2G[NO^{*}] - G[H_{2,gas}] \quad (40)$$

$$\Delta H^{\ddagger} = H[TS^{2*}] + H[NO_{gas}] - 2H[NO^{*}] - H[H_{2,gas}] \quad (41)$$

$$\Delta S^{\ddagger} = S[TS^{2*}] + S[NO_{gas}] - 2S[NO^{*}] - S[H_{2,gas}] \quad (42)$$

$\Delta G^{\ddagger}$ (and $\Delta H^{\ddagger}$ and $\Delta S^{\ddagger}$) values can be calculated (from DFT); they do not depend on the free energies of H^* and HNO^* intermediates. These DFT-derived $\Delta G^{\ddagger}$, $\Delta H^{\ddagger}$, and $\Delta S^{\ddagger}$ values are compared to experimental values in Table 4 for several possible kinetically-relevant transition states and indicate that H^*-assisted NO activation routes have much lower $\Delta G^{\ddagger}$ than those without H^*-involvement and are closer to the $\Delta G^{\ddagger}$ values observed experimentally, as described in detail in Section 3.5.

Previous studies remain inconclusive about whether H^* exists at kinetically-significant coverages during NO/H_2 reactions. Here, both Eqs. (22) and (23) indicate that H^* exists as a MASI and that the fractional H^* coverage (θ_H) is given by:

$$\theta_H = \frac{\beta\chi}{1+\beta\chi} \quad (43)$$

with β given by Eq. (24) and χ defined as:

$$\chi = \frac{P_{H_2}^{0.5}}{P_{NO}} \quad (44)$$

when NO^* and H^* are the MASI and they compete for binding sites on a uniform (Langmuirian) surface. Fig. 10 shows the change in H^* coverage (with NO^* at all other sites) as a function of χ, indicating that at large χ values ($\geqslant 5\ kPa^{-0.5}$), the surface becomes predominantly covered by H^* at 423 K, in contradiction to previous conclusions for $NO–H_2$ reactions on Rh [5].

3.5. Mechanism of N–O activation during $NO–H_2$ reactions

The elementary steps proposed in previous studies for $NO–H_2$ reactions on Pt and Rh catalysts include direct NO^* dissociation (Eq. (3)) [5,17], NO^*–NO^* reactions to form N_2O (Eq. (4)) [7] and NO dissociation after the addition of one H-atom to NO^* (Eq. (6)) [5,9]. None of these proposals can be reconciled with the observed first-order rate dependence on H_2 at low H_2 pressures (Fig. 4a) or with the constant asymptotic rates reached at high H_2 pressures (Fig. 5b). Several sequences of elementary steps involving two H-atoms at the kinetically-relevant transition state are consistent with the functional form of Eqs. (22) and (23). These sequences include the following: (i) quasi-equilibrated HNO^* formation and subsequent irreversible reactions with H^* to form $^*HNOH^*$ (Eqs. (10) and (11)) or (ii) quasi-equilibrated NOH^* formation (Eq. (5)) with subsequent irreversible H^* addition (ii-a) at the N-atom of NOH^* to form $^*HNOH^*$:

$$NOH^* + H^* \rightarrow {}^*HNOH^* \quad (45)$$

or (ii-b) at the O-atom of NOH^*, concomitantly with N–O cleavage to form N^* and H_2O:

$$NOH^* + H^* \rightarrow N^* + H_2O \quad (46)$$

If $^*HNOH^*$ formation steps (Eq. (8) or Eq. (45)) are quasi-equilibrated, their subsequent dissociation to form NH^* and OH^* (Eq. (12)) or N^* and H_2O:

$${}^*HNOH^* \rightarrow N^* + {}^* + H_2O \quad (47)$$

would become the sole kinetically-relevant step. These routes cannot be distinguished by experiment, but may be discerned by DFT estimates of the contributions by these parallel routes. The respective $\Delta G^{\ddagger}$ and $\Delta H^{\ddagger}$ values can also be compared with values determined from measured rate constants (α, discussed in Section 3.4). DFT methods are also used to examine routes that are inconsistent with the functional form of the measured rate equation (Eq. (23)); these mechanisms include NO^*-assisted NO^* activation (Eq. (4)), direct NO^* dissociation (Eq. (3)), NOH^* dissociation (Eq. (6)), and HNO^* dissociation:

$$HNO^* + {}^* \rightarrow NH^* + O^* \quad (48)$$

None of these alternate routes, however, can account for the observed effects of H_2 and NO pressures on reaction rates, as discussed above. DFT calculations were carried out on extended Pt (1 1 1) surfaces, the most thermodynamically stable surface, because weak effects of cluster size on turnover rates (Section 3.7) suggest that reactivity and mechanistic details are not sensitive to the identity of exposed planes and the coordination of their exposed atoms. NO^* coverages vary from 0.10 to 0.83 over the range of χ values (2–51) examined here (423 K; Fig. 10), making DFT calculations at each coverage and the large number of configurations of H^* and NO^* at each coverage impractical. Calculations were first carried out at 3/9 ML coverages of spectator NO^*. Calculations were then repeated at 0, 2/9, 4/9, and 5/9 ML spectator NO^* for kinetically-relevant steps in each NO^* activation route

Table 4
Summary of NO* activation routes.

Route	Kinetically-relevant step	Rate equation	α	$\Delta H^{\ddagger}$ [a] kJ mol^{-1}	$\Delta G^{\ddagger}$ [a,b,c] kJ mol^{-1}	KIE
NO*-assisted	$2NO^* \rightarrow O^* + {}^* + N_2O(g)$	$r_{NO} = \frac{\alpha P_{NO}^2}{[P_{NO}+\beta P_{H_2}^{0.5}]^2}$	$\alpha = k_4$	203	190	1
Direct	$NO^* \rightarrow N^* + O^*$	$r_{NO} = \frac{\alpha P_{NO}}{\left[P_{NO}+\beta P_{H_2}^{0.5}\right]^2}$	$\alpha = \frac{k_3}{K_{NO}}$	315	248	1
H*-assisted via NOH*	$NOH^* \rightarrow N^* + OH^*$	$r_{NO} = \frac{\alpha P_{NO} P_{H_2}^{0.5}}{\left[P_{NO}+\beta P_{H_2}^{0.5}\right]^2}$	$\alpha = \frac{k_6 K_5 K_{H_2}^{0.5}}{K_{NO}}$	181	151	0.53
H*-assisted via HNO*	$HNO^* + H^* \rightarrow {}^*HNOH^*$	$r_{NO} = \frac{\alpha P_{NO} P_{H_2}}{\left[P_{NO}+\beta P_{H_2}^{0.5}\right]^2}$	$\alpha = \frac{k_{11} K_{10} K_{H_2}}{K_{NO}}$	122	114	1.46
	$^*HNOH^* \rightarrow NH^* + OH^*$	$r_{NO} = \frac{\alpha P_{NO} P_{H_2}}{\left[P_{NO}+\beta P_{H_2}^{0.5}\right]^2}$	$\alpha = \frac{k_{12} K_{11} K_{10} K_{H_2}}{K_{NO}}$	150	149	0.63
Kinetic Data	–	$r_{NO} = \frac{\alpha P_{NO} P_{H_2}}{\left[P_{NO}+\beta P_{H_2}^{0.5}\right]^2}$		48	108	1.38 ± 0.35

[a] Values determined at a coverage of 3/9 ML of spectator NO* species, 423 K.
[b] Values determined using a standard pressure of 1 bar.
[c] $\Delta G^{\ddagger}$ is given by Eq. (33) for the kinetic data, and equations for $\Delta G^{\ddagger}$ calculated from DFT each mechanism are found in Eqs. (55), (64), and (71), for direct and H-assisted NO* activation routes, respectively.

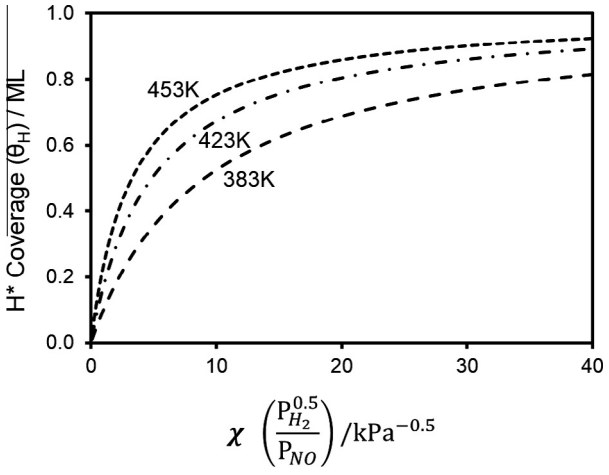

Fig. 10. H* coverage (with NO* at all other sites) as a function of χ (Eq. (43)), determined from β values regressed from kinetic data at 383–453 K (Eq. (23)) (0.6%Pt/Al_2O_3, 4.4 nm average particle diameter).

to determine the extent to which NO* coverages influence the mechanistic conclusions.

3.5.1. NO-assisted NO* activation

NO* dissociation can be assisted by a vicinal NO* to form O* and N_2O (Eq. (4)) with an intrinsic free energy barrier ($\Delta G_{act,4}$) of 190 kJ mol^{-1} at 3/9 ML spectator NO* (5/9 ML total NO*) (Fig. 11). NO* first desorbs and reacts with a vicinal NO* to form an *ONNO* species, which undergoes N–O bond activation to form N_2O and O* (DFT structures at multiple NO* coverages provided in SI, Fig. S15–S16). If these steps occurred in practice (even with such large barriers), O* must then react with H* to form OH* and then H_2O*:

$$O^* + H^* \rightarrow OH^* + {}^* \quad (49)$$

$$OH^* + H^* \rightarrow H_2O^* + {}^* \quad (50)$$

in sequential steps with respective ΔG_{act} barriers of 64 and 11 kJ mol^{-1} (Fig. 11). NO*-assisted NO* dissociation steps (Eq. (4)) are irreversible because N_2O desorbs immediately upon formation and does not inhibit NO reduction or undergo secondary reactions (Section 3.1), and thus the sole kinetically-relevant step. In this case, the rate equation:

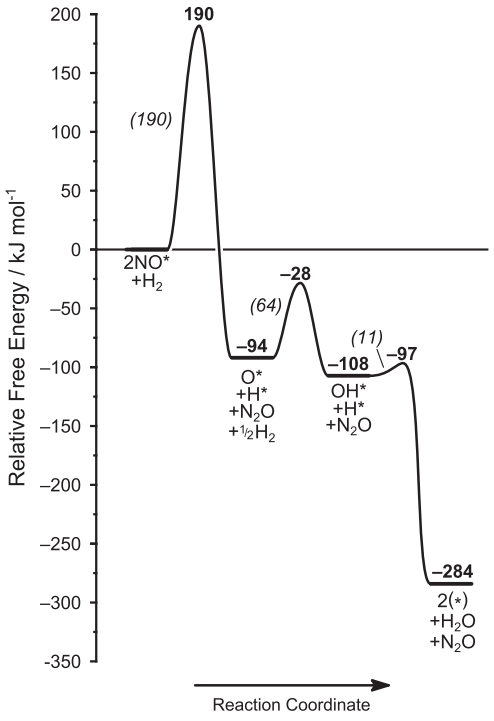

Fig. 11. Free energy reaction coordinate diagram for NO*-assisted NO* activation at 3/9 ML spectator NO* (5/9 ML total NO*). NO*-assisted NO* activation to form N_2O is irreversible and the kinetically-relevant step for this NO activation mechanism. Italicized energy values in parentheses represent intrinsic forward or reverse free energy barriers, bold energy values represent energies relative to a NO*-covered surface.

$$r_{NO} = \frac{k_4 P_{NO}^2}{\left[P_{NO} + \beta P_{H_2}^{0.5}\right]^2} \quad (51)$$

depends inversely on H_2 pressure, reflecting the occurrences of all H*-addition steps only after the sole kinetically-relevant step. Consequently, the high intrinsic barrier and irreversible nature of NO*-assisted NO* activation renders the route inconsequential in NO–H_2 reactions catalyzed by on Pt surfaces.

3.5.2. Direct NO* dissociation

NO* can also dissociate by reacting with vicinal vacancies (*) to form N* and O* (Eq. (3)), instead of reacting with vicinal NO* species to form N* and N_2O. This step has a large intrinsic free energy barrier ($\Delta G_{act,3}$ = 239 kJ mol^{-1}; 3/9 ML spectator NO* coverages) and occurs by NO* leaning over to coordinate the O* to the metal surface in either an atop or bridge site, depending on NO* coverage (DFT structures at multiple NO* coverages provided in SI, Figs. S17 and S18). Its reverse barrier ($\Delta G_{act,-3}$ = 123 kJ mol^{-1}) is much larger than the barrier for reactions that consume N* (via reactions with NO* to form N_2O; 85 kJ mol^{-1}) or to consume O* (via reactions with H* to form H_2O; 97 kJ mol^{-1}), indicating that NO dissociation steps are irreversible (Fig. 12) and kinetically-relevant for this route. NO–H_2 rates via direct NO* dissociation are inversely-dependent on H_2 pressure:

$$r_{NO} = \frac{\alpha P_{NO}}{\left[P_{NO} + \beta P_{H_2}^{0.5}\right]^2} \quad (52)$$

$$\alpha = \frac{k_3}{K_{NO}} \quad (53)$$

because H* is a MASI and is not involved in the kinetically-relevant step for direct NO* dissociation. The inverse-dependence of NO–H_2 rates on H_2 pressure is in contradiction to measured rates which increase with H_2 pressure at low H_2 pressures and approach a zero-order dependence on H_2 at high H_2 pressures (Figs. 4 and 5); no inhibition of NO–H_2 rates by H_2 was observed in this study (0.1–0.5 kPa NO, 1–760 kPa H_2, 383–453 K). $\Delta G^{\ddagger}$ values for the lumped α parameter that describes this route (Eq. (53)) depend on the free energies for NO desorption ($-\Delta G_{NO,ads}$) and on the intrinsic free energy barrier for Eq. (3) ($\Delta G_{act,3}$):

$$\Delta G^{\ddagger} = \Delta G_{act,3} - \Delta G_{ads,NO} \quad (54)$$

This last equation becomes:

$$\Delta G^{\ddagger} = G\left[N{-}O^{\ddagger **}\right] + G[NO(g)] - 2G[NO^*] \quad (55)$$

when rewritten in terms of the properties of the relevant intermediates; the $\Delta G^{\ddagger}$ value given by DFT methods is 248 kJ mol^{-1} at 3/9 ML of spectator NO* (Fig. 13). As in the case of NO*-assisted NO* activation, the large barrier and irreversibility of direct NO* dissociation render it unproductive in NO–H_2 reaction rates. The ratio of reaction rates via direct NO* dissociation and NO*-assisted NO activation:

$$\frac{r_{NO\text{-direct}}}{r_{NO-NO}} = \frac{k_3}{k_4 K_{NO} P_{NO}} = \frac{1}{P_{NO}} e^{\left(\frac{\Delta G_{act,3} - \Delta G_{ads}^{\ddagger}}{RT}\right)} \quad (56)$$

is inversely proportional to NO pressure, indicating that direct NO* dissociation will be most relevant at low NO pressure. The ratio, however, is 8×10^{-5} at the lowest NO pressure in this work (0.1 kPa), indicating that direct NO* dissociation does not occur, even in the absence of H_2.

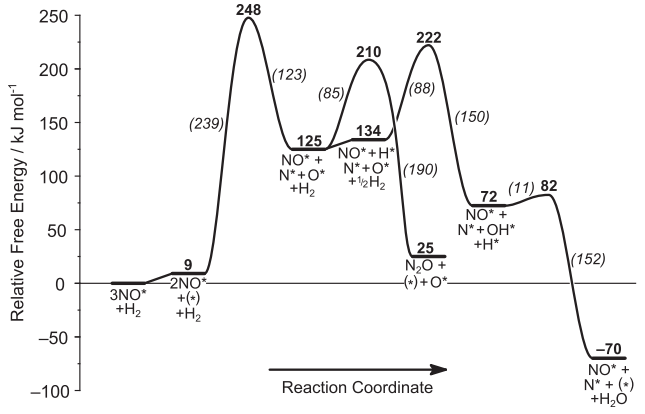

Fig. 12. Free energy reaction coordinate diagram for direct NO* dissociation at 3/9 ML spectator NO* (4/9 ML total NO*). Direct NO* dissociation is irreversible and the kinetically-relevant step for this NO activation mechanism. Italicized values in parenthesis represent intrinsic forward or reverse free energy barriers, bold values represent energies relative to a NO*-covered surface.

3.5.3. H*-assisted NO* activation and NOH* dissociation routes

NO activation via formation and dissociation of NOH* was previously proposed as a route in NO–H_2 reactions on Pt and Rh catalysts [5,9–11] with the formation of NOH* as the sole kinetically-relevant step. Our DFT calculations show that NO* reacts with H* to form NOH* with an intrinsic free energy barrier ($\Delta G_{act,5}$) of 72 kJ mol^{-1} at 3/9 ML spectator NO* (Fig. 13). The reaction proceeds via NO* leaning toward H* which is in an atop position in the transition state (DFT structures at multiple NO* coverages provided in SI, Figs. S19–S21). The ΔG to form NOH* from NO* and ½H_2(g) is 65 kJ mol^{-1} (Fig. 13), indicating that it is a minority species present at coverages undetectable by spectroscopic methods. NOH* can then dissociate by reacting with a vacant site to form N* and OH* ($\Delta G_{act,6}$ = 87 kJ mol^{-1}) or with H* to form N* and H_2O* (via concerted O–H formation and N–O cleavage; Eq. (46); $\Delta G_{act,46}$ = 115 kJ mol^{-1}). This latter barrier is smaller than that for *HNOH* formation via H* addition to NOH* ($\Delta G_{act,45}$ = 124 kJ mol^{-1}), making *HNOH* formation via NOH* (Eq. (45)) unlikely to contribute to NO activation rates. The reversibility of these NOH* formation steps depends on the relative rates of its reverse reaction (r_{-5}) and the combined rates of NOH* dissociation (Eq. (6)) and N* and H_2O formation from NOH* (Eq. (46)):

$$\frac{r_{-5}}{r_6 + r_{46}} = \frac{k_{-5}[NOH^*][*]}{(k_6[NOH^*][*]) + (k_{46}[NOH^*][H^*])} = \frac{k_{-5}[*]}{k_6[*] + k_{46}[H^*]} \quad (57)$$

This equation can be rewritten in terms of free energies and H_2 pressures (in bar units):

$$\frac{r_{-5}}{r_6 + r_{46}} = \frac{e^{\left(\frac{-\Delta G_{act,-5}}{RT}\right)}}{e^{\left(\frac{-\Delta G_{act,6}}{RT}\right)} + e^{\left(\frac{-\left(\Delta G_{act,46} + 0.5\Delta G_{ads,H_2}\right)}{RT}\right)} P_{H_2}^{0.5}} \quad (58)$$

A comparison of the rates of NOH* dissociation (Eq. (6)) and H*-addition to NOH* to form N* and H_2O (Eq. (46)):

$$\frac{r_6}{r_{46}} = \frac{e^{\left(\frac{-\Delta G_{act,6}}{RT}\right)}}{e^{\left(\frac{-\left(\Delta G_{act,46} + 0.5\Delta G_{ads,H_2}\right)}{RT}\right)} P_{H_2}^{0.5}} \quad (59)$$

indicates that $r_6 \gg r_{46}$ at any H_2 pressure below ~10^{11} bar, because the free energy barrier for NOH* dissociation to N* and OH* ($\Delta G_{act,6}$ = 87 kJ mol^{-1}) is much smaller than the sum of free energy terms representing NOH* consumption via Eq. (46) (138 kJ mol^{-1}). Eq. (58) can then be simplified to:

$$\frac{r_{-5}}{r_6} = \frac{e^{\left(\frac{-\Delta G_{act,-5}}{RT}\right)}}{e^{\left(\frac{-\Delta G_{act,6}}{RT}\right)}} \quad (60)$$

This ratio has a very large value of ~10^7 at 423 K because the free energy barrier for NOH* dissociation to H* and NO* (the reverse of NOH* formation) ($\Delta G_{act,-5}$ = 29 kJ mol^{-1}) is much smaller than that for NOH* dissociation to N* and OH* ($\Delta G_{act,6}$ = 87 kJ mol^{-1}), indicating that NOH* formation is quasi-equilibrated. NOH* dissociation is irreversible and is the kinetically-relevant step for H*-assisted NO* activation routes via NOH*, leading to a rate equation:

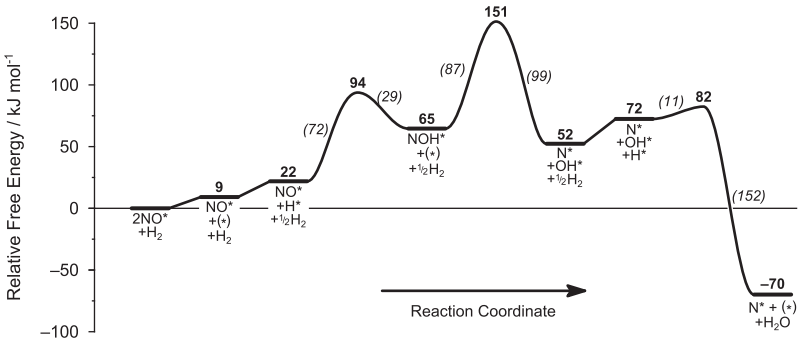

Fig. 13. Free energy reaction coordinate diagram for H*-assisted NO* activation and NOH* dissociation at 3/9 ML spectator NO* (4/9 ML total NO*). NOH* formation is quasi-equilibrated and its dissociation is irreversible and the kinetically-relevant step for this NO* activation mechanism. Italicized energy values in parentheses represent intrinsic forward or reverse free energy barriers, bold energy values represent energies relative to a NO*-covered surface.

$$r_{NO} = \frac{\alpha P_{NO} P_{H_2}^{0.5}}{\left[P_{NO} + \beta P_{H_2}^{0.5}\right]^2} \tag{61}$$

$$\alpha = \frac{k_6 K_5 K_{H_2}^{0.5}}{K_{NO}} \tag{62}$$

Eq. (61) does not fit the measured kinetic data as well as rate equations with a first-order dependence in H_2 in the numerator (Eq. (21) or Eq. (22)), and is inconsistent with the approach to zero order in H_2 dependence observed in Fig. 5b, as discussed earlier. The effective activation free energy ($\Delta G^{\ddagger}$) for this mechanism depends on the intrinsic free energy barrier for NOH* dissociation, the reaction energy for NOH* formation, and the H_2 and NO adsorption free energies:

$$\Delta G^{\ddagger} = \Delta G_{act,6} + \Delta G_{rxn,5} + 1/2\Delta G_{ads,H2} - \Delta G_{ads,NO} \tag{63}$$

Substituting the free energies of intermediates into Eq. (63) leads to:

$$\Delta G^{\ddagger} = G[\mathrm{N{-}OH}^{\ddagger **}] + G[\mathrm{NO(g)}] - 2G[\mathrm{NO}^*] - \frac{1}{2}G[\mathrm{H_2(g)}] \tag{64}$$

which gives a value of $\Delta G^{\ddagger}$ of 151 kJ mol^{-1} at a coverage of 3/9 ML of spectator NO* (Fig. 13). This $\Delta G^{\ddagger}$ is much lower than those for direct or NO*-assisted NO activation (248 and 190 kJ mol^{-1}, respectively) and is similar to the $\Delta G^{\ddagger}$ for H*-assisted NO activation via *HNOH* (discussed below). This mechanism, however, is inconsistent with observed normal kinetic isotope effects (discussed below) and rates which become constant with increasing H_2 pressure (Fig. 2b), as discussed above.

3.5.4. H*-assisted NO* activation and *HNOH* dissociation routes

NO* can also undergo H*-assisted NO* activation via HNO* intermediates rather than via NOH* intermediates. NO* can react with H* to form HNO* (Eq. (10)) with an intrinsic free energy barrier ($\Delta G_{act,10}$) of 77 kJ mol^{-1}. The transition state involves atop bound NO* and H* combining to form the N–H bond with HNO* ultimately binding atop through the N-atom (DFT structures at multiple NO* coverages provided in SI, Figs. S21 and S22). HNO* can then dissociate to form NH* and O* (Eq. (48)) with a $\Delta G_{act,48}$ value of 135 kJ mol^{-1} or react with H* on the surface to form *HNOH* with a $\Delta G_{act,11}$ value of 40 kJ mol^{-1}. The transition state during *HNOH* formation involves HNO* in a bridging or atop site reacting with vicinal atop H*, similar to the NOH* formation geometry, (DFT structures at multiple NO* coverages provided in SI, Figs. S23 and S24). The ΔG to form HNO* and *HNOH* from NO* and stoichiometric amounts of H_2(g) are 71 and 68 kJ mol^{-1} (Fig. 14), indicating that they are minority species undetectable by spectroscopic methods because of their low coverages. The large ΔG to form HNO* (71 kJ mol^{-1}) and NOH* (65 kJ mol^{-1}) also indicate that direct H-transfer reactions between these intermediates to form *HNOH* are unlikely, due to their low concentrations. *HNOH* then dissociates to form NH* and OH* (Eq. (12)) with a lower barrier ($\Delta G_{act,12}$ = 81 kJ mol^{-1}) than that for N* and H_2O formation ($\Delta G_{act,47}$ = 111 kJ mol^{-1}), indicating that Eq. (47) does not contribute to measured rates at these temperatures. The barrier for the reverse of *HNOH* formation reaction ($\Delta G_{act,-11}$ = 46 kJ mol^{-1}) is much lower than for *HNOH* dissociation ($\Delta G_{act,12}$ = 81 kJ mol^{-1}), consistent with quasi-equilibrated *HNOH* formation steps, but the difference between these two barriers (35 kJ mol^{-1}) decreases with increasing NO* coverage (6 kJ mol^{-1} and −5 kJ mol^{-1} at 4/9 and 5/9 ML spectator NO*, respectively), indicating *HNOH* formation may not be quasi-equilibrated at all NO* coverages. The reversibility of HNO* formation depends on the ratio of its reverse rate (r_{-10}) to the sum of the rates of *HNOH* dissociation to NH* and OH* (Eq. (12)) and of HNO* dissociation to NH* and O* (Eq. (47)):

$$\frac{r_{-10}}{r_{12} + r_{48}} = \frac{k_{-10}[*]}{k_{12}K_{11}[H^*] + k_{48}[*]} \tag{65}$$

Eq. (64) can be rewritten in terms of free energy differences and the H_2 pressure (in units of bar):

$$\frac{r_{-10}}{r_{12} + r_{48}} = \frac{e^{\left(\frac{-\Delta G_{act,-10}}{RT}\right)}}{e^{\left(\frac{-\left(\Delta G_{act,12} + \Delta G_{rxn,11} + 0.5\Delta G_{ads,H_2}\right)}{RT}\right)} P_{H_2}^{0.5} + e^{\left(\frac{-\Delta G_{act,48}}{RT}\right)}} \tag{66}$$

The ratio of rates of HNO* consumption via *HNOH* (Eq. (12)) to HNO* dissociation (Eq. (48)):

$$\frac{r_{12}}{r_{48}} = \frac{e^{\left(\frac{-\left(\Delta G_{act,12} + \Delta G_{rxn,11} + 0.5\Delta G_{ads,H_2}\right)}{RT}\right)} P_{H_2}^{0.5}}{e^{\left(\frac{-\Delta G_{act,48}}{RT}\right)}} \tag{67}$$

is very large (100 or higher) at H_2 pressures greater than 1.1×10^{-10} bar because the free energy barrier to dissociate HNO* ($\Delta G_{act,48}$ = 135 kJ mol^{-1}) is much larger than the sum of free energy terms representing HNO* consumption via *HNOH* ($\Delta G_{act,12} + \Delta G_{rxn,11} + 0.5\Delta G_{ads,H_2}$ = 78 kJ mol^{-1}). Eq. (66) can then be simplified to:

$$\frac{r_{-10}}{r_{12}} = \frac{e^{\left(\frac{-\Delta G_{act,-10}}{RT}\right)}}{e^{\left(\frac{-\left(\Delta G_{act,12} + \Delta G_{rxn,11} + 0.5\Delta G_{ads,H_2}\right)}{RT}\right)} P_{H_2}^{0.5}} \tag{68}$$

and this ratio is very large (1000 or higher) at H_2 pressures less than 2.8×10^4 bar at 423 K since because the reverse barrier for HNO* formation ($\Delta G_{act,-10}$ = 28 kJ mol^{-1}) is much less than the sum of free energy terms representing HNO* consumption via *HNOH*

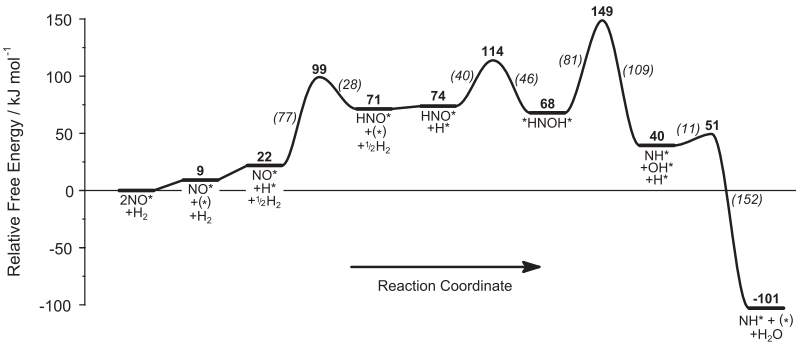

Fig. 14. Free energy reaction coordinate diagram for H*-assisted NO* activation and *HNOH* dissociation at 3/9 ML spectator NO* (4/9 ML total NO*). HNO* and *HNOH* formations are quasi-equilibrated, *HNOH* dissociation is irreversible and the DFT-predicted kinetically-relevant step for this NO* activation mechanism. Italicized energy values in parentheses represent intrinsic forward or reverse free energy barriers, bold energy values represent energies relative to a NO*-covered surface.

(78 kJ mol^{-1}). Thus, H*-assisted NO* activation via HNO* proceeds through kinetically-relevant *HNOH* dissociation steps (Eq. (12)), which leads to a rate equation with a numerator proportional to H_2 pressure in the rate equation (Eq. (23)) with a kinetic rate constant (α):

$$\alpha = \frac{k_{12}K_{11}K_{10}K_{H_2}}{K_{NO}} \tag{69}$$

The effective activation free energy ($\Delta G^{\ddagger}$) for H*-assisted NO* activation via HNO* depends on the intrinsic free energy barrier for *HNOH* dissociation, the reaction energies for HNO* and *HNOH* formation, and the H_2 and NO adsorption free energies.

$$\Delta G^{\ddagger} = \Delta G_{act,12} + \Delta G_{rxn,11} + \Delta G_{rxn,10} + \Delta G_{ads,H2} - \Delta G_{ads,NO} \tag{70}$$

Substituting the free energies for each of the intermediates involved leads to:

$$\Delta G^{\ddagger} = G[HN{-}OH^{\ddagger **}] + G[NO(g)] - 2G[NO^*] - G[H_2(g)] \tag{71}$$

which gives a $\Delta G^{\ddagger}$ value of 149 kJ mol^{-1} at a coverage of 3/9 ML of spectator NO* (Fig. 14). The mechanism, in which *HNOH* formation or dissociation is the kinetically-relevant step (depending on the coverage of NO*, as discussed later), is consistent with measured rates (Eq. (23)) and has a $\Delta G^{\ddagger}$ (149 kJ mol^{-1}) significantly lower than NO* activation routes without H*-assistance (248 and 190 kJ mol^{-1} for Eqs. (3) and (4), respectively).

3.5.5. Summary of NO* activation mechanisms

The four routes of NO* activation considered here and are summarized in Table 4. These distinct routes are denoted as (i) NO*-assisted NO* activation; (ii) direct NO* dissociation; (iii) H*-assisted NO* activation via NOH* (which then dissociates); and (iv) H*-assisted NO* activation via HNO* (which activates N–O after forming *HNOH*). For each of these, the reversibility of each step was evaluated and kinetically-relevant steps were identified based on DFT-derived free energies. Each of these sequences gives a distinct rate equation and allows DFT calculations of their effective activation free energies ($\Delta G^{\ddagger}$) and kinetic isotope effects (KIE).

The ratio of the rate of H*-assisted NO activation via *HNOH* to NOH* dissociation is given by taking the ratios of their respective rate equations (Eq. (23) and (61), respectively):

$$\frac{r_{HNOH}}{r_{NOH}} = \frac{k_{12}K_{11}K_{10}K_{H_2}^{0.5}P_{H_2}^{0.5}}{k_6K_5} \tag{72}$$

This ratio can be rewritten in terms of free energies:

$$\frac{r_{HNOH}}{r_{NOH}} = \frac{e^{\left(\frac{-\left(\Delta G_{act,12}+\Delta G_{rxn,11}+\Delta G_{rxn,10}+0.5\Delta G_{ads,H_2}\right)}{RT}\right)}P_{H_2}^{0.5}}{e^{\left(\frac{-\left(\Delta G_{act,6}+\Delta G_{rxn,5}\right)}{RT}\right)}} \tag{73}$$

The difference in the sum of free energy terms for *HNOH* dissociation ($\Delta G_{act,12} + \Delta G_{rxn,11} + \Delta G_{rxn,10} + 0.5\Delta G_{ads,H_2}$ = 127 kJ mol^{-1}) and the sum of free energy terms for NOH* dissociation ($\Delta G_{act,6} + \Delta G_{rxn,5}$ = 129 kJ mol^{-1}) is small and indicates that the ratio is equal to 1 at a H_2 pressure of 23 kPa, as shown in Fig. 15. This critical H_2 pressure, however, depends upon the coverage of NO* in the DFT model, as discussed below, and such small differences in activation free energies (2 kJ mol^{-1}) are likely smaller than the uncertainties from DFT associated with determining vibrational frequencies of adsorbed species (and transition states) accurately. We conclude here that DFT suggests that both mechanisms contribute to observed NO reduction rates during NO–H_2 reactions on Pt, however, as discussed in Section 3.6, a comparison of measured kinetic isotope effects and those calculated from DFT for both routes suggest that *HNOH* formation, not NOH* dissociation, is the kinetically-relevant step for NO activation during NO–H_2 reactions on Pt.

The prevalence of H*-assisted over direct NO* dissociation routes observed at 3/9 ML of spectator NO* was confirmed by DFT calculations at coverages of 0, 2/9, 4/9, and 5/9 ML spectator NO*. The effective activation free energy ($\Delta G^{\ddagger}$) for NO*-assisted NO* activation, direct NO* dissociation, and H*-assisted NO* activation via NOH* and *HNOH* dissociation are shown in Fig. 16 at 0/9–5/9 ML of spectator NO*. The $\Delta G^{\ddagger}$ values for H*-assisted NO* activation are much smaller than for NO*-assisted and direct NO* activation routes at all coverages. The differences in $\Delta G^{\ddagger}$ values for *HNOH* formation and dissociation decrease with increasing coverage and indicate that DFT-predicted $\Delta G^{\ddagger}$ suggests that both the formation and dissociation of *HNOH* are kinetically-relevant steps for the H*-assisted NO* activation via *HNOH* mechanism. Kinetic isotope effects, which differ for these two steps, indicate that *HNOH* formation is the sole kinetically-relevant step (Section 3.6).

The differences in $\Delta G^{\ddagger}$ values between kinetically-relevant steps involving NOH* and *HNOH* are small at 0–5/9 ML of spectator NO*, leading to similar DFT-predicted rates for both H-assisted NO* activation mechanisms. H*-assisted NO activation via NOH*, however, leads to a half-order dependence in H_2 in the numerator of the rate equation (Eq. (26)); this dependence contradicts the asymptotic constant rates observed at high H_2 pressures (Fig. 5b), indicating that H*-assisted NO activation via NOH* does not contribute to measured NO–H_2 reaction rates.

The values of $\Delta G^{\ddagger}$ decrease with increasing NO* coverage (Fig. 16), while the differences in $\Delta G^{\ddagger}$ between the various mechanisms remains unchanged. This decrease in $\Delta G^{\ddagger}$ values with increasing NO* coverage predominantly reflects an increase in $\Delta G_{ads,NO}$ (weakening of NO* binding strength) with increasing coverage, making the formation of a vacancy, necessary for the formation of the kinetically-relevant transition state at high coverage. $\Delta G_{ads,NO}$ is +117 kJ mol^{-1}, however, at 5/9 ML of spectator NO*,

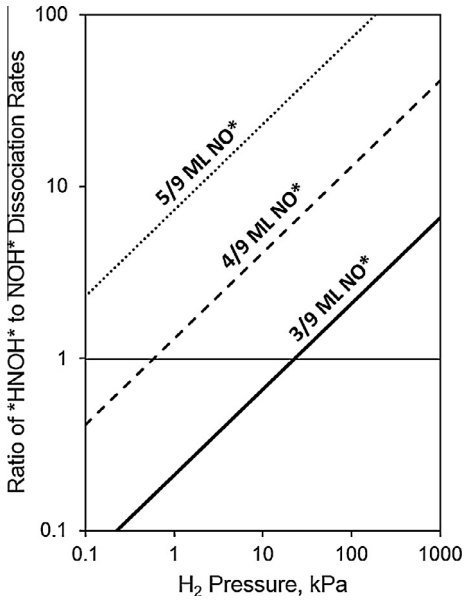

Fig. 15. Ratio of *HNOH* to NOH* dissociation rates (Eq. (72)) based on DFT-predicted $\Delta G^{\ddagger}$ at a coverage of 3/9–5/9 ML of spectator NO* species.

corresponding to a very small adsorption constant ($K_{NO} = 3.6 \times 10^{-15}$ at 423 K), indicating that such coverages are unlikely on (1 1 1) crystal surfaces or large (1 1 1) facets of multicrystalline particles. Lower NO* coverages (4/9 ML spectator NO*, 6/9 ML total NO*) give a $\Delta G_{ads,NO}$ value of +6 kJ mol^{-1}. This $\Delta G_{ads,NO}$ value indicates that NO* adsorption may be favorable at such coverages because the $\Delta G_{ads,NO}$ values in this work are underestimated due to the lack of van der Waals interactions (causing $\Delta H_{ads,NO}$ to be underestimated) and the inability of DFT to accurately capture the anharmonic motions of weakly-adsorbed species (causing $\Delta S_{ads,NO}$ to be overestimated). The $\Delta G^{\ddagger}$ is 91 kJ mol^{-1} at this coverage, in fairly good agreement with experiments (108 kJ mol^{-1}).

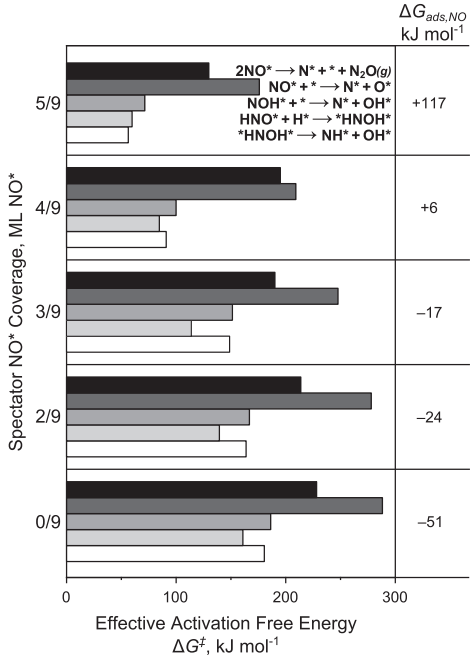

Fig. 16. Effective activation free energies ($\Delta G^{\ddagger}$) at various NO* spectator coverages (0–5/9 ML of spectator NO*). $\Delta G^{\ddagger}$ decrease with increasing coverage due to the increase in NO adsorption free energy ($\Delta G_{ads,NO}$, shown on the right). Despite the change in barriers with increasing coverage, at all coverages it is clear that H*-assisted NO* activation reactions have lower $\Delta G^{\ddagger}$ than those for direct or NO*-assisted NO* activation.

3.6. Measured and DFT-derived H/D kinetic isotope effects

H_2/D_2 kinetic isotope effects were measured by comparing rates and rate constants (α and β) obtained from NO–H_2 and NO–D_2 reactions at 423 K. NO activation rates are higher with H_2 than D_2, (Fig. 17); thus, kinetic isotope effects are larger than unity. Regression of these data to Eq. (23) shows good agreement between measured and predicted rates for both H_2 and D_2 co-reactants (parity plot in SI, Fig. S8) and gives values (with 95% confidence intervals shown) of α of 0.30 ± 0.04 s^{-1} and β of 0.32 ± 0.03 kPa$^{0.5}$ for NO/D_2 reactants and 0.42 ± 0.05 s^{-1} and 0.21 ± 0.03 kPa$^{0.5}$ for NO/H_2 reactants. The isotope effect for β (0.64 ± 0.14) reflects the thermodynamics of H_2/D_2 dissociative adsorption:

$$\frac{\beta_H}{\beta_D} = \left(\frac{K_{H_2}}{K_{D_2}}\right)^{0.5} \tag{74}$$

The corresponding $\left(\frac{K_{H_2}}{K_{D_2}}\right)$ value (0.41 ± 0.18) suggests an inverse thermodynamic isotope effect. K_{H_2} and K_{D_2} values from H_2 and D_2 adsorption isotherms on Pt/Al_2O_3 (3.4 nm average diameter) give a $\left(\frac{K_{H_2}}{K_{D_2}}\right)$ value of 0.66 [50], consistent with the inverse effect observed here.

The H_2/D_2 isotope effects for α were larger than unity (1.38 ± 0.32), indicating that $\Delta G^{\ddagger}_H$ values are slightly smaller than $\Delta G^{\ddagger}_D$ values (by 0.6 kJ mol^{-1} at 453 K).

$$\frac{\alpha_H}{\alpha_D} = e^{\left(\frac{\Delta G^{\ddagger}_D - \Delta G^{\ddagger}_H}{RT}\right)} \tag{75}$$

Frequency calculations for each deuterated and undeuterated species and transition states were used to determine $\Delta G^{\ddagger}$ values with H_2 and D_2 as reactants, which can be used to determine kinetic isotope effects on α (Eq. (75)). The $\Delta G^{\ddagger}$ for H*-assisted NO activation via NOH* was calculated to be 2.2 kJ mol^{-1} lower for D_2 than for H_2, leading to a large inverse isotope effect (0.53), inconsistent with the measured value (1.38 ± 0.32, Table 4). Similarly, *HNOH* dissociation, one of the possible kinetically-relevant steps for H*-assisted NO activation via *HNOH*, gives a large inverse isotope effect (0.63), which originates from the difference in the reaction free energy to form *HNOH* from NO* and H_2 (Eq. (76), 121 kJ mol^{-1}) and that to form *DNOD* from NO* and D_2 (118 kJ mol^{-1}):

$$2NO^{*} + H_2(g) \rightarrow {}^{*}HNOH^{*} + NO(g) \tag{76}$$

indicating that this isotopic effect is primarily a thermodynamic isotopic effect on the equilibrium constants for *HNOH* formation (K_{11}) and HNO* formation (K_{10}). The large difference between the calculated isotope effect for *HNOH* dissociation (0.63) and that measured (1.38) appears to rule it out as the kinetically-relevant step. The $\Delta G^{\ddagger}$ for H*-addition to HNO* to form *HNOH*, in contrast, increases by 1.3 kJ mol^{-1} leading to a normal isotope effect (1.46), much closer to the measured isotope effect (1.38), indicating that it is the likely kinetically-relevant step.

3.7. Effect of Pt coordination on NO conversion rate

Pt/Al_2O_3 catalysts with Pt dispersions of 0.63, 0.25 and 0.08 (1.5, 4 and 10 nm mean diameter) were prepared using methods reported above and used to determine the effects of Pt cluster size on α and β values.

The data in this study indicate that the relevant kinetic (α, Eq. (24)) and thermodynamic (β, Eq. (25)) parameters are only weakly affected by Pt dispersion or cluster size (Fig. 18). Thus, concomitant

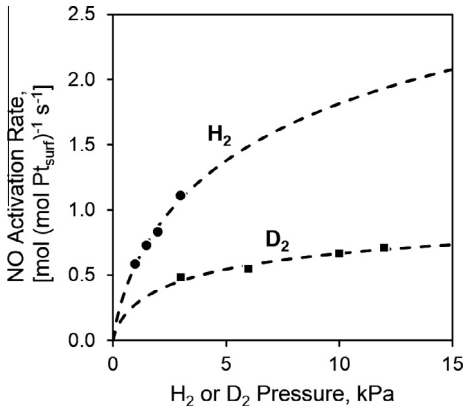

Fig. 17. NO activation rates as a function of H_2 (•) or D_2 (▪) pressure at 423 K on 0.6% Pt/Al_2O_3 (4.4 nm average particle diameter), 1–3 kPa H_2, 3–12 kPa D_2, 0.3 kPa NO, 5–25 $cm^3\ s^{-1}\ g^{-1}$. Dashed lines indicate regression of Eq. (23) to this data and data at 0.1, 0.2, 0.4, and 0.5 kPa NO. Parity plot for the regressions found in SI (Fig. S25).

changes in the average coordination of exposed Pt atoms do not appear to influence significantly the grouping of equilibrium and rate constants in α or the relative binding properties of NO* and H* (β).

Similar structure insensitivity was observed for CO oxidation on Pt particles during which surfaces are saturated with CO*, as a consequence of simultaneous increasing of both the rate and equilibrium constants for surface reaction and CO adsorption, as the coordination of exposed Pt atoms decreases with decreasing particle size [47]. This was attributed to, in part, a weakening of the non-uniformity of sites on the Pt particle due to adsorbate and surface restructuring at high CO* coverages to alleviate the strain induced by strong adsorbate–adsorbate repulsions [47]. In contrast, structure sensitivity was observed for NO reduction by CO on Pt and Rh catalysts, where the NO turnover rates increase with Pt and Rh cluster size [15,30,51]. The increase in NO–CO rates on larger particles was attributed to a weakening of NO* and CO* binding energies on such particles, making it easier to form the necessary ensembles of metal atoms required for NO–CO activation.

Experimental [30,31,51] and theoretical [26,29,47] studies have demonstrated that equilibrium constants for both H_2 and NO increase with decreasing Pt particle size because of stronger Pt–H and Pt–NO bonds at coordinatively unsaturated corner and edge sites [26,29,30,32]. So, the structure insensitivity observed for β is attributed to a compensation effect, as a consequence of similar coordination and Pt particle size effects on H_2 and NO adsorption equilibrium constants. The net reaction corresponding to β (Fig. 8) replaces one Pt–N bond with one Pt–H bond, and since β is structure insensitive, this predicts that the effect of Pt particle size (and metal atom coordination) is similar between Pt–N and Pt–H bonds at high NO* and H* coverages, possibly due to the same surface restructuring phenomena observed during CO oxidation on Pt at high CO* coverage which homogenizes the previously distinct surface sites by rounding out the particle to alleviate adsorbate–adsorbate repulsions [47].

Weak effects of Pt coordination on α (Fig. 18a) can be explained from the combination of particle size effects on the constants comprising α (Eq. (24)). Since β is structure-insensitive as explained above and the H_2 adsorption equilibrium constant (K_{H_2}) increases with decreasing Pt cluster size [29,32], the product ($k_{11}K_{10}$) of the rate constant for *HNOH* formation (Eq. (11)) and the equilibrium constant for HNO* formation (Eq. (10)) should increase as Pt particle size increases to result in little overall change in α. Stronger Pt–NO and Pt–H bonds on corners and edges of small clusters decrease the reaction free energy for *HNO* formation, thus leading to higher K_{HNO} values for larger Pt particles. Similarly, the intrinsic free energy barriers for *HNOH* formation from *HNO* (Eq. (12)) are expected to be lower on larger Pt particles because of a weaker Pt–H bond which is broken during the reaction, thus increasing k_{HNO-H} with increasing Pt particle size. The net reaction corresponding to α (Fig. 8) replaces two NO* species on the catalyst surface with a kinetically-relevant transition state bound in a di-σ manner, which results in a net exchange of a Pt–N bond with a Pt–H bond (as does β). The structure insensitivity of α again predicts that Pt–N and Pt–H bonds change similarly with particle size (and therefore metal atom coordination) at high coverages of NO* and H*.

Ultimately, α and β are nearly independent of particle size because they represent sequences of elementary steps, which do not result in a net change in the number of adsorbate–metal bonds. Since both result in the net exchange of a Pt–N bond with a Pt–H bond (Fig. 8), their weak dependence on particle size indicates that the difference between Pt–N and Pt–H bond strength is invariant of coordination number, i.e., that Pt–N and Pt–H bonds are similarly affected by particle size.

4. Conclusions

N_2O, N_2, and NH_3 are primary products of NO reduction with H_2 on Pt/Al_2O_3 as they do not react in secondary steps nor inhibit NO conversion rates. Relative rates of H_2–D_2 scrambling and NO

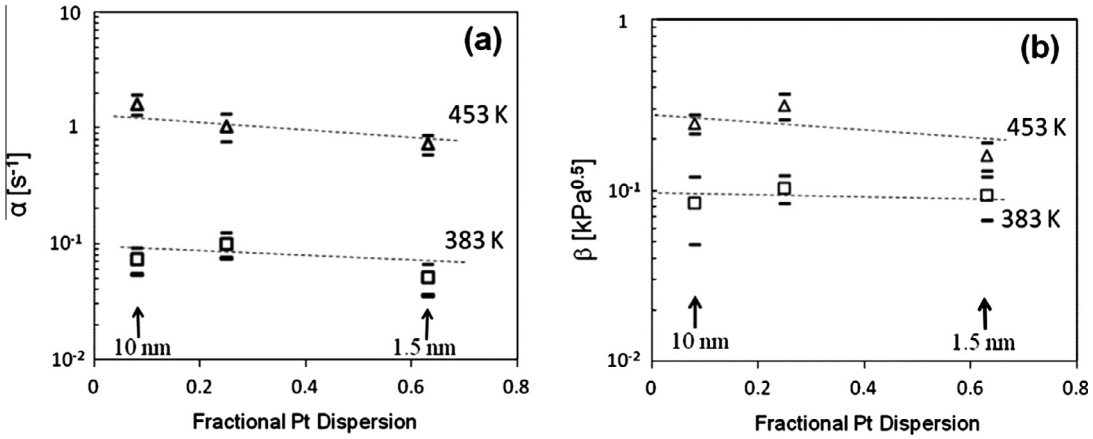

Fig. 18. Values of NO reduction rate parameters α (Eq. (24)) and β (Eq. (25)) on Pt/Al_2O_3 catalysts with 0.08–0.63 fractional Pt dispersion.

reduction suggest that H_2 dissociation is quasi-equilibrated at NO pressures and temperatures relevant to NO reduction. NO^* inhibits HD formation, indicating that it competes for sites with H^* and D^* on the catalyst surface. The rate equation (Eq. (23)) is in good agreement with measured kinetic data and is consistent with a DFT-predicted mechanism in which NO^* is activated through a H-assisted mechanism. The kinetically-relevant step is predicted to be H^*-addition to HNO^* to form $^*HNOH^*$ by rates independent of H_2 pressure at high H_2 pressure, calculations of effective free energy barriers from DFT at 6/9 ML NO^*, as well as measured and DFT-predicted kinetic isotope effects. NO reduction turnover rates on Pt/Al_2O_3 were essentially independent of surface Pt coordination for Pt cluster size range between 1.5 and 10 nm, and this structure insensitivity is attributed to compensation between effects of Pt cluster size on the constants comprised in the kinetic and thermodynamic parameters of the rate equation (Eqs. (23)–(25)).

NO^* decomposes in the absence of H_2 via bimolecular reactions, in which two NO^* species react on the metal surface to form O^* and N_2O in a mechanism similar to that observed during CO oxidation on Pt surfaces, in which O_2 is activated by reaction with a vicinal CO^* to form O^* and CO_2 [47]. These reactions occur on surfaces saturated in one or more reactant, typical of steady-state catalysis where high coverages reduce the available number of vacancies for direct bond activation and thereby reinforce the preference for bimolecular reactions. When H_2 is present, NO prefers to react with H^* to form $^*HNOH^*$ prior to N–O bond activation at any coverage, similar to mechanisms observed for Fischer–Tropsch synthesis in which CO reacts with H^* to form $^*HCOH^*$ prior to C–O bond activation on Fe, Co [22] and Ru [23,24] surfaces nearly saturated with CO^*. Similarly, O_2 initially forms OOH^* or $^*HOOH^*$ intermediates prior to O–O bond activation on Pd, Pt and Au surfaces when H_2 or H_2O is present [48,49]. NO, CO, and O_2 contain double or triple bonds, which are weakened by initial reactions with H^* that increase metal atom coordination, facilitating bond activation.

Acknowledgments

Financial support from GM and technical discussions with Dr. Wei Li (GM) are gratefully acknowledged. Computational resources provided by XSEDE (CHE130022). RJ acknowledges financial support from Red Doctoral REDOC.CTA, MINEDUC Project UCO1202 at Universidad de Concepcion and FONDECYT Grant 1101005, Chile, during sabbatical research at UC Berkeley.

Appendix A. Supplementary material

Supplementary data associated with this article can be found, in the online version, at http://dx.doi.org/10.1016/j.jcat.2014.07.012.

References

[1] C.N. Costa, P.G. Savva, C. Andronikou, P.S. Lambrou, K. Polychronopoulou, V.C. Belessi, V.N. Stathopoulos, P.J. Pomonis, A.M. Efstathiou, J. Catal. 209 (2002) 456–471.
[2] I. Nova, L. Lietti, L. Castoldi, E. Tronconi, P. Forzatti, J. Catal. 239 (2006) 244–254.
[3] M. Engelmann-Pirez, P. Granger, G. Leclercq, Catal. Today 107–108 (2005) 315–322.
[4] C.N. Costa, A.M. Efstathiou, J. Phys. Chem. B 108 (2004) 2620–2630.
[5] W.C. Hecker, A.T. Bell, J. Catal. 92 (1985) 247–259.
[6] R. Burch, M.D. Coleman, J. Catal. 208 (2002) 435–447.
[7] A.A. Shestov, R. Burch, J.A. Sullivan, J. Catal. 186 (1999) 362–372.
[8] R. Burch, A.A. Shestov, J.A. Sullivan, J. Catal. 186 (1999) 353–361.
[9] F. Dhainaut, S. Pietrzyk, P. Granger, J. Catal. 258 (2008) 296–305.
[10] F. Dhainaut, S. Pietrzyk, P. Granger, Appl. Catal. B 70 (2007) 100–110.
[11] F. Dhainaut, S. Pietrzyk, P. Granger, Catal. Today 119 (2007) 94–99.
[12] K. Tomishige, K. Asakura, Y. Iwasawa, J. Catal. 157 (1995) 472–481.
[13] A. Kumar, V. Medhekar, M.P. Harold, V. Balakotaiah, Appl. Catal. B 90 (2009) 642–651.
[14] A.A. Chin, A.T. Bell, J. Phys. Chem. 87 (1983) 3700–3706.
[15] R. Burch, P.J. Millington, A.P. Walker, App. Catal. B 4 (1994) 65–94.
[16] B. Frank, G. Emig, A. Renken, Appl. Catal. B 19 (1998) 45–57.
[17] W.C. Hecker, A.T. Bell, J. Catal. 84 (1983) 200–215.
[18] B.E. Nieuwenhuys, Adv. Catal. 44 (1999) 259–328.
[19] C.A. de Wolf, B.E. Nieuwenhuys, Catal. Today 70 (2001) 287–300.
[20] H. Hirano, T. Yamada, K.I. Tanaka, J. Siera, B.E. Nieuwenhuys, Stud. Surf. Sci. Catal. 75 (1993) 345–357.
[21] H. Hirano, T. Yamada, K.I. Tanaka, J. Siera, P. Cobden, B.E. Nieuwenhuys, Surf. Sci. 262 (1992) 97–112.
[22] M. Ojeda, R. Nabar, A. Nilekar, A. Ishikawa, M. Mavrikakis, E. Iglesia, J. Catal. 272 (2010) 287–297.
[23] B. Loveless, C. Buda, M. Neurock, E. Iglesia, J. Am. Chem. Soc. 135 (2013) 6107–6121.
[24] D. Hibbitts, B. Loveless, M. Neurock, E. Iglesia, Ang. Chem. Int. Ed. 52 (2013) 12273–12278.
[25] R. Jiménez, D. Hibbitts, M. Yoshimura, E. Iglesia, unpublished results.
[26] Q. Ge, M. Neurock, J. Am. Chem. Soc. 126 (2004) 1551–1559.
[27] A. Amirnazmi, M. Boudart, J. Catal. 39 (1975) 383–394.
[28] M.J. Mummey, L.D. Schmidt, Surf. Sci. 109 (1981) 29–42.
[29] D.C. Ford, Y. Xu, M. Mavrikakis, Surf. Sci. 587 (2005) 159–174.
[30] J. Nováková, L. Kubelková, App. Catal. B 14 (1997) 273–286.
[31] B.M. Weiss, E. Iglesia, J. Phys. Chem. C 113 (2009) 13331–13340.
[32] C.H. Bartholomew, Hydrogen Adsorption on Supported Noble Metals and Its Use in Determining Metal Dispersion, in: J.J. Spivey, S.K. Agarwal (Eds.), Catalysis, A Specialist Periodical Report, vol. 11, Royal Society of Chemistry, 1994.
[33] M. Johansson, O. Lytken, I. Chorkendorff, J. Chem. Phys. 128 (2008) 034706.
[34] G. Kresse, J. Furthmüller, Comput. Mater. Sci. 6 (1996) 15–50.
[35] G. Kresse, J. Furthmüller, Phys. Rev. B: Condens. Matter 54 (1996) 11169–11186.
[36] G. Kresse, J. Hafner, Phys. Rev. B: Condens. Matter 47 (1993) 558–561.
[37] G. Kresse, J. Hafner, Phys. Rev. B: Condens. Matter 49 (1994) 14251–14269.
[38] P.E. Blöchl, Phys. Rev. B: Condens. Matter 50 (1994) 17953–17979.
[39] G. Kresse, D. Joubert, Phys. Rev. B: Condens. Matter 59 (1999) 1758–1775.
[40] B. Hammer, L. Hansen, J.K. Nørskov, Phys. Rev. B: Condens. Matter 59 (1999) 7413–7421.
[41] J. Perdew, K. Burke, M. Ernzerhof, Phys. Rev. Lett. 77 (1996) 3865–3868.
[42] Y. Zhang, W. Yang, Phys. Rev. Lett. 80 (1998) 890.
[43] H.J. Monkhorst, J.D. Pack, Phys. Rev. B: Condens. Matter 13 (1976) 5188–5192.
[44] G. Henkelman, H.A. Jónsson, J. Chem. Phys. 113 (2000) 9978–9985.
[45] H.A. Jónsson, G. Mills, K.W. Jacobsen, Nudged Elastic Band Method for Finding Minimum Energy Paths of Transitions, World Scientific, 1998.
[46] G. Henkelman, H.A. Jónsson, J. Chem. Phys. 111 (1999) 7010–7022.
[47] A.D. Allian, K. Takanabe, K.L. Fujdala, X. Hao, T.J. Truex, J. Cai, C. Buda, M. Neurock, E. Iglesia, J. Am. Chem. Soc. 133 (2011) 4498–4517.
[48] B. Zope, D. Hibbitts, M. Neurock, R. Davis, Science 330 (2010) 74.
[49] D. Hibbitts, M. Neurock, J. Catal. 299 (2013) 261–271.
[50] M. García-Diéguez, E. Iglesia, unpublished results.
[51] C.H.F. Penden, D.N. Belton, S.J. Schmieg, J. Catal. 155 (1995) 204–218.